IVYSPRING INTERNATIONAL PUBLISHER

Nanotheranostics

2026; 10: 317-338. doi: 10.7150/ntno.137024

Research Paper

Liposomal Co-delivery of Resveratrol and Coumarin-6 Enhances Radiosensitization across Microbial and Melanoma Systems

Nitisha Beniwal✉, Chandra Lekha Putta✉, Thaninki Lakshmi Srujana✉, Aravind Kumar Rengan✉

Department of Biomedical Engineering, Indian Institute of Technology Hyderabad, Kandi, Sangareddy, Telangana-502285, India.

✉ Corresponding authors: Aravind Kumar Rengan (aravind@bme.iith.ac.in); Nitisha Beniwal (bm22resch11005@iith.ac.in); Chandra Lekha Putta (bm22resch11001@iith.ac.in); Thaninki Lakshmi Srujana (bm24resch11005@iith.ac.in).

© 2026 The Author(s). This is an open access article distributed under the Creative Commons Attribution 4.0 International Licence, subject to the Publisher's Terms of Use at https://ivyspring.com/terms.

Received: 2026.04.30; Accepted: 2026.08.10; Published: 2026.10.25

Abstract

Efficacy of radiotherapy is often limited by intrinsic cellular radioresistance, requiring the development of biomaterial-based radiosensitizers that can enhance therapeutic outcomes across diverse biological systems. Herein, we report a multifunctional liposomal nanoplatform co-encapsulating Resveratrol, a redox-active radiosensitizer, and Coumarin-6, a fluorescent probe enabling real-time tracking and showing mild bio-activity (Res-Cou6@NPs, ~200 nm), designed for efficient delivery and enhanced radiotherapeutic performance. The nanoplatform exhibited high physicochemical stability, favorable biocompatibility, and efficient cellular internalization. To establish a robust and predictive evaluation strategy, we employed the radiation-resistant bacterium *Deinococcus radiodurans* as a stringent biological model. Treatment with Res-Cou6@NPs significantly enhanced X-ray-induced cytotoxicity in this system, as evidenced by reduced survival and increased membrane damage, indicating disruption of intrinsic radioresistance mechanisms. Extending these findings to mammalian models, the nanoplatform markedly sensitized B16F10 melanoma cells to radiation by promoting intracellular reactive oxygen species generation, inducing mitochondrial dysfunction, and enhancing cell death, while exhibiting minimal toxicity toward normal fibroblasts. Furthermore, Res-Cou6@NPs effectively suppressed cancer cell migration, clonogenic survival, and three-dimensional spheroid invasion, and synergistically amplified radiation-induced cytotoxicity. Collectively, these results highlight the potential of this liposomal nanoplatform as an effective radiosensitizing biomaterial and establish a cross-kingdom evaluation framework that bridges microbial and mammalian systems for predictive assessment of radiotherapeutic nanomedicines.

Keywords: resveratrol, coumarin-6, liposomal nanoformulation, radioresistance, *Deinococcus radiodurans*, radiosensitization

1. Introduction

Melanoma is an aggressive and life-threatening skin malignancy that, although representing only approximately 1% of all skin cancer diagnoses, is responsible for the vast majority of skin cancer-related fatalities worldwide. According to global cancer statistics from 2022, an estimated 331,722 new melanoma cases were reported globally, resulting in nearly 58,667 deaths, underscoring the substantial mortality associated with this disease [1]. The high fatality rate of melanoma is primarily attributed to its strong metastatic propensity and the poor clinical outcomes observed once the cancer disseminates to distant organs, highlighting the urgent need for more effective therapeutic interventions [2,3].

Radiotherapy represents an important treatment option for melanoma, particularly in cases involving unresectable tumors and metastatic disease. Although it can achieve effective local tumor control, melanoma has long been regarded as intrinsically radioresistant. This resistance is largely attributed to proficient

deoxyribonucleic acid (DNA) damage repair processes, hypoxic tumor microenvironments, and the activation of oncogenic survival signaling pathways [2–4]. Consequently, radiotherapy alone often yields limited therapeutic benefit, necessitating combination strategies or the incorporation of radiosensitizing agents to enhance tumor responsiveness and improve clinical outcomes. In recent years, nanoparticle-based drug delivery platforms have garnered considerable attention in melanoma treatment due to their ability to enhance intratumoral drug accumulation via both passive and active targeting, improve the solubility of hydrophobic therapeutics, and protect payloads from premature degradation [5–7]. Despite these advantages, several obstacles hinder their clinical translation, including limited tumor penetration, premature drug release, off-target toxicity, and rapid clearance. Addressing these limitations is essential to fully realize the therapeutic potential of nanoparticle-mediated delivery systems in melanoma management [8].

Resveratrol (3,5,4′-trihydroxy-trans-stilbene), a naturally occurring polyphenol abundant in grapes and berries, has gained considerable attention due to its multifaceted anticancer properties, including pro-apoptotic, anti-angiogenic, anti-metastatic, and anti-inflammatory activities [9]. These effects are mediated through modulation of key oncogenic signaling pathways such as PI3K/Akt, MAPK/ERK, STAT3, and NF-κB, leading to inhibition of tumor cell proliferation and induction of mitochondrial-mediated apoptosis. Importantly, resveratrol has also been identified as an effective radiosensitizer, capable of enhancing radiation-induced DNA damage, elevating intracellular reactive oxygen species (ROS) levels, suppressing DNA repair mechanisms, and reducing hypoxia-associated radioresistance via downregulation of HIF-1α [10]. Despite these promising attributes, the clinical translation of resveratrol is severely limited by its extremely low aqueous solubility (<0.05 mg mL^{-1}), rapid hepatic metabolism, chemical instability, and very poor oral bioavailability (<1%), resulting in insufficient therapeutic concentrations at tumor sites. To address these limitations, nanocarrier-based delivery systems have been widely explored to improve resveratrol solubility, protect it from premature metabolism, and enhance tumor accumulation. Coumarin-6, a highly hydrophobic fluorescent dye with strong green emission, high photostability, and excellent quantum yield, is frequently employed as a tracer molecule for real-time visualization of nanoparticle uptake, intracellular trafficking, and biodistribution [11]. In addition to its imaging capability, coumarin-6 has been reported to induce mild oxidative stress and mitochondrial dysfunction in cancer cells, thereby complementing therapeutic payloads [12]. The co-delivery of resveratrol and coumarin-6 within a single nanoplatform thus offers a rational theranostic strategy, enabling simultaneous enhancement of anticancer and radiosensitizing efficacy while providing real-time tracking of nanoparticle behavior at the cellular level [13].

Liposomal encapsulation using soya phosphatidylcholine (Soya PC) offers an effective strategy to co-deliver these hydrophobic agents in a biocompatible and clinically relevant platform [14–17]. The amphiphilic lipid bilayer of Soya PC-based liposomes allows simultaneous incorporation of Resveratrol and Coumarin-6, protects them from degradation, improves systemic circulation time, and enhances tumor-targeted delivery while minimizing off-target toxicity [18]. Furthermore, their structural similarity to biological membranes reduces immune clearance and promotes passive targeting along with stimuli-responsive drug release. Collectively, this design addresses key clinical challenges by improving bioavailability, enabling combinational therapy, reducing systemic toxicity, and enhancing the efficacy of radiotherapy [19–21].

In addition to material design, the selection of appropriate biological models is critical for evaluating radiosensitizer performance. Conventional mammalian systems often fail to fully capture the limits of intrinsic radioresistance. In this context, extreme radioresistant organisms such as *Deinococcus radiodurans* provide a stringent and biologically relevant platform to assess the ability of nanomaterials to overcome radiation tolerance under severe stress conditions.

In this work, we designed and systematically characterized a phosphatidylcholine-based liposomal nanocarrier co-encapsulating Resveratrol and Coumarin-6 for enhanced radiosensitization. The formulation was evaluated for its physicochemical properties, colloidal stability, and controlled drug release behavior under physiologically relevant conditions, along with its biocompatibility and therapeutic efficacy. To establish a more stringent evaluation framework, the radiosensitizing performance of the nanoplatform was first assessed in an extreme radioresistant model, followed by validation in melanoma systems. This integrated approach enables a more robust assessment of nanomedicine performance across biological complexity and highlights the potential of liposomal delivery systems for improving radiotherapeutic outcomes.

2. Materials & Methods

2.1 Chemicals

Dimethyl sulfoxide (DMSO), ethanol, methanol, chloroform, and Nile Red were acquired from SRL Chemicals Limited, India. Dulbecco's Modified Eagle Medium (DMEM), Penicillin-streptomycin (Pen-strep) solution, trypsin-EDTA, phosphate-buffered saline (PBS), fetal bovine serum (FBS), and Thiazolyl Blue Tetrazolium Bromide (MTT) were obtained from HiMedia Laboratories, India. Soyabean Phosphatidylcholine (Soya PC), Hoechst, 2',7'-Dichlorodihydrofluorescein Diacetate (DCFDA), 4',6-diamidino-2-phenylindole (DAPI), fluorescein diacetate (FDA), propidium iodide (PI), acridine orange/ethidium bromide (AO/EtBr), Resveratrol (Res), and Coumarin 6 (Cou6) were acquired from Sigma-Aldrich Private Limited, India. Syringe filters (0.2 µm) were obtained from Sartorius (Carrigtwohill, Ireland). Phospho-Histone H2AX-S139 Rabbit pAB (AP0099) and ABflo® 488-conjugated Goat anti-Rabbit IgG (H+L) (AS053), were acquired from ABclonal biomolecular solutions, India. Milli-Q water was utilized from the Millipore system located in Billerica, MA. All other reagents employed were of analytical grade.

2.2 Bacterial Culture & Maintenance

Bought *Deinococcus radiodurans* culture from The Microbial Type Culture Collection and Gene Bank (MTCC), India. One colony from a Luria-Bertani Agar (LB) plate was taken out and inoculated it into LB broth. The broth was then kept at 37 °C until the culture reached an Optical Density $(OD)_{600}$ of 1.0.

2.3 Cell Lines Maintenance and Incubation

The National Centre for Cell Science (NCCS) in Pune, India, gave us mouse embryonic fibroblast cell lines L929 and NIH3/T3. The melanoma cell line (B16F10), the murine mammary carcinoma cell line (4T1), and the human cervical cancer cell line (HeLa) were obtained from the Centre for Cellular and Molecular Biology (CCMB) in Hyderabad, India. The L929, B16F10, HeLa, and NIH3/T3 cell lines were grown and maintained in high-glucose DMEM. The 4T1 cell line, on the other hand, was cultured in RPMI media with 10% (v/v) FBS, 1% L-glutamine, and 100 U/mL of streptomycin/penicillin at 37 °C in a 5% humidified CO_2 incubator.

2.4 X-ray Irradiation Specifications

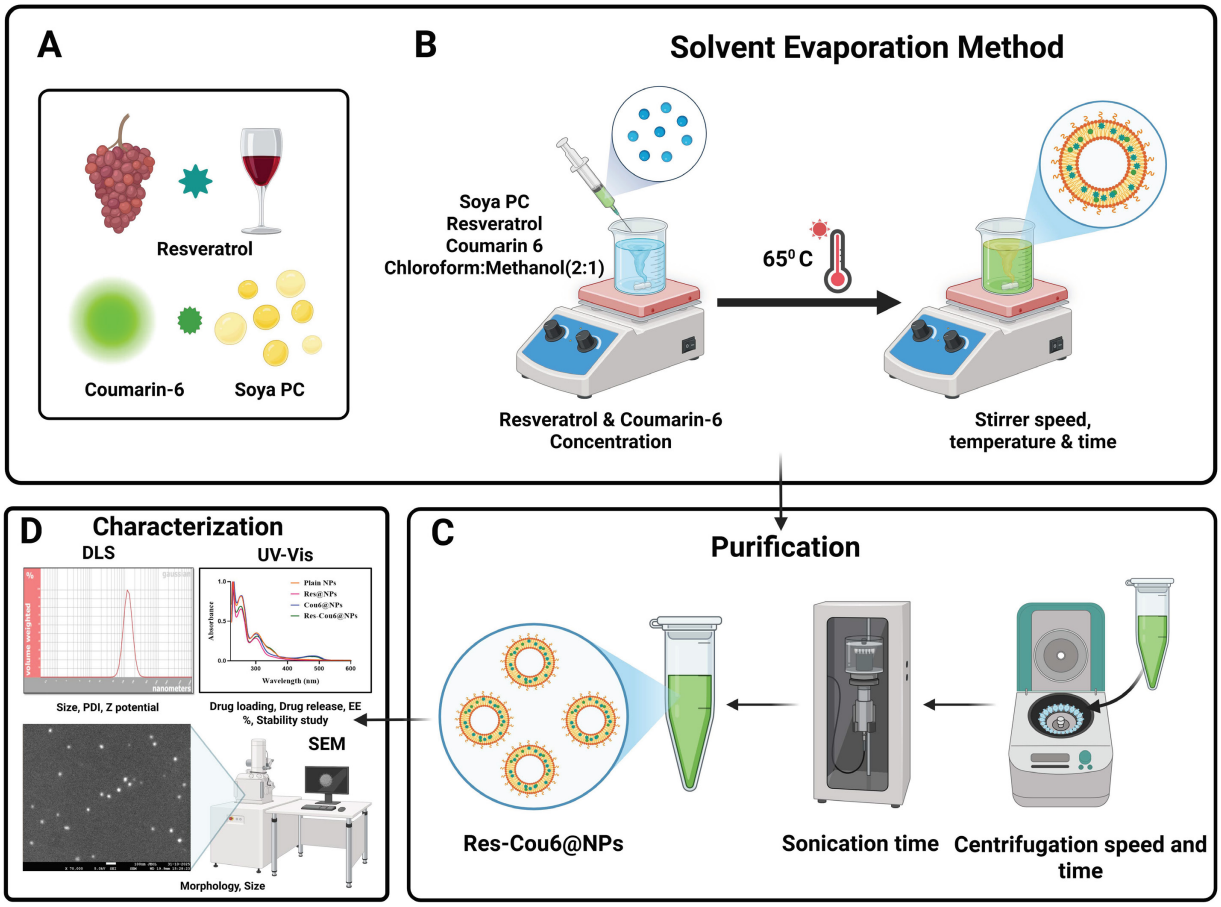
An X-RAD 225iR X-ray irradiator (Precision X-Ray Inc., USA) was used to irradiate the cells. Cells subjected to a cumulative radiation exposure of 4 Gy at a dose rate of 0.8 Gy·min^{-1} over 5 minutes. The X-ray tube voltage used by the irradiator was 225 kVp. The irradiation system's license number was 25-GICCOMM-1407537. To guarantee precise dose distribution, the institutional radiation facility regularly calibrated and maintained the irradiator before use.

3. Methodology

3.1 Synthesis of Nanoparticles (NPs)

The solvent evaporation technique exhibits clear advantages compared to thin-film hydration in liposomal production, providing improved control over particle size distribution and increased encapsulation efficiency. Thin-film hydration generally results in heterogenous multilamellar vesicles (MLVs), whereas solvent evaporation reliably yields smaller, monodisperse unilamellar vesicles. Comparative analyses demonstrate enhanced drug stability for particular drug delivery applications [22,23]. Soya PC was dissolved in a 2:1 chloroform: methanol solution and swiftly injected into preheated warmed distilled water at 65 ^{0}C (Milli-Q grade). The subsequent dilution of organic solvents below a critical concentration threshold (≤7.5% v/v of total formulation volume) triggers lipid self-assembly in the aqueous phase. The fast dilution causes lipid precipitation, resulting in the formation of planar bilayer fragments that enclose aqueous regions. The evaporation of the solvent subsequently promotes the union of fragments, resulting in the creation of closed unilamellar vesicles (SUVs). Surpassing the 7.5% organic solvent threshold or introducing it into a significant excess of aqueous phase leads to diverse MLV populations. Post-synthesis, Res-Cou6@NPs were centrifuged (16,500 rpm, 25 °C, 20 min) to pellet down the liposomes. The pellet was resuspended in 1 mL Milli-Q water, sonicated for 10 min under ice-cooling to ensure equal dispersion, and kept at -4 °C for subsequent investigation, as shown in Scheme 1.

The same procedure was uniformly employed to synthesize three nanoparticle variants (NPs): Plain NPs (devoid of therapeutic and fluorescent agents), Resveratrol-loaded NPs (Res@NPs), and Coumarin-6-loaded NPs (Cou6@NPs). For intracellular tracking, Nile red-encapsulated Res-Cou6@NPs were prepared by dropwise addition of Nile red (dissolved in methanol) to the aqueous phase during assembly. All formulations were purified via centrifugation (16,500 rpm, 25 °C, 20 min), resuspended in Milli-Q water, sonicated on ice (10 min), and stored at -4 °C.



Scheme 1. Synthesis and characterization of Res-Cou6@NPs.

3.2 Characterization of Nanoparticles

Synthesized nanoparticles were characterized by physiochemical analysis. Ultraviolet-visible (UV-Vis) spectroscopy (Shimadzu UV-1800, Japan) was employed to quantify absorbance profiles, whereas fluorescence spectra were obtained using a fluorescence spectrophotometer (Shimadzu RF-6000, Japan). The hydrodynamic diameter, polydispersity index (PDI), and zeta (ζ)-potential were assessed using dynamic light scattering (DLS). Morphological characteristics were analyzed by scanning electron microscopy (SEM). Functional group analysis was conducted using Fourier-transform infrared spectroscopy (FTIR: Shimadzu FT/IR-4600 type A, Japan). While the crystallographic structure was evaluated using X-ray diffraction (XRD: Rigaku Smart Lab, Japan) employing Cu Kα radiation (λ = 1.5406 Å).

3.3 Drug Release and Stability Studies of Res-Cou6@NPs

The *in vitro* release profile of the nanoparticles was assessed utilizing the dialysis bag method at two pH levels (5.2 and 7.4) in PBS. The drug release was quantified utilizing a UV-Visible spectrophotometer at consistent time intervals (1, 2, 4, 6, 12, 24, and 48 h). Stability experiments of the synthesized nanoparticles were conducted at 4 °C in both water and PBS. The mean hydrodynamic size, PDI, zeta potential, and encapsulation efficiency (EE%) of the drug and dye were measured and calculated over a period of 28 days.

3.4 Encapsulation Efficiency Determination

Encapsulation efficiency of Res and Cou6 was quantified using UV-Vis spectrophotometry. Following nanoparticle synthesis, free (unencapsulated) Res and Cou6 were separated via centrifugation or filtration. The supernatant/filtrate containing unbound drug was analysed, with concentration determined against a pre-established standard calibration curve [24]. The percentage of encapsulation efficiency is calculated using the following formula:

$$EE\ \% = [(\text{Total drug} - \text{Free drug}) / \text{Total drug}] \times 100.$$

3.5 Bacterial Clonogenic Survival Assay

The radiosensitization of the synthesised nanoparticles (Plain NPs, Res@NPs, Cou6@NPs, and

Res-Cou6@NPs) was assessed using the spot assay at serial dilutions ranging from 10^{-0} to 10^{-12} and followed by colony formation assay. *Deinococcus radiodurans* cultures of 5×10^{-5} - 1×10^{-6} CFU/mL from the 24 h incubated bacterial samples were treated with nanoparticles at a concentration of 100 µg/mL, which was selected based on prior biocompatibility studies on normal NIH3/T3 and L929 cell lines. The treated bacterial samples along with untreated (Control) were divided into two sets: one set was exposed to X-ray irradiation of 50 Gy after 4 hours of incubation, while the other set was kept non-irradiated. Both sets were further incubated overnight, then serially diluted 10 times with MH Broth, and 5 µL of sample from each dilution was spotted on the MH Agar plate for analysing radiosensitization efficacy of the nanoparticles.

For the bacterial spread assay/colony formation Assay, aliquots of 30 µL from the samples at dilutions of 10^{-2}, 10^{-8}, and 10^{-12} were spread on MH Agar plates, followed by overnight incubation to evaluate colony-forming ability.

3.6 Radiation-Induced Bacterial Cell Damage Assay

The Live/Dead assay was conducted utilizing SYTO9/PI staining to qualitatively evaluate the cytotoxicity of the synthesized nanoparticles. Both the X-ray irradiation and non-irradiated experimental groups underwent staining following 24 hours of incubation at 37 °C. A 20 µL aliquot of each sample was stained with SYTO9/PI, placed onto a glass slide with a coverslip, and incubated for 20 minutes. The staining facilitated distinct identification of live and dead cells, with viable cells emitting green fluorescence (SYTO9) and non-viable cells emitting red fluorescence (PI). Cellular pictures were subsequently acquired utilizing a Zoe microscope.

3.7 In vitro Studies

3.7.1 Biocompatibility Studies

The biocompatibility of Plain NPs, Res@NPs, Cou6@NPs, and Res-Cou6@NPs was evaluated using the MTT assay with L929 and NIH3/T3 cell lines. Cells were seeded at a density of 1×10^4 cells/well in 96-well plates and incubated for 24 h at 37 °C. Subsequent to incubation, cells were exposed to nanoparticles (1, 2, 5, 10, 25, 50, 100 µg/mL) and incubated for 24 h, was then introduced with MTT (5 mg/10 mL) to each well and incubated for 3 hours. The resultant formazan crystals were solubilized with DMSO, and absorbance was quantified using a multi-mode plate reader (BIORAD Microplate Reader) at 570 nm (primary) and 630 nm (reference) [25].

3.7.2 Cytotoxicity Studies

The MTT assay was employed to evaluate the cell viability of Plain NPs, Res@NPs, Cou6@NPs, and Res-Cou6@NPs in relation to HeLa, 4T1, and B16F10 melanoma cell lines. Briefly, 1×10^4 cells/well were seeded in 96-well plates using cell-specific growth media and incubated for 24 h. Subsequently, cells were treated with nanoparticles (1, 2, 5, 10, 25, 50, 100 µg/mL) in fresh media for 24 h. MTT reagent (5 mg/10mL) was then added and incubated for 3 h. After careful removal of supernatant, 100 µL DMSO was added to solubilize the developed formazan crystals. Absorbance was quantified at 570 nm (primary) and 630 nm (reference) using a multi-mode plate reader (BIORAD Microplate Reader) [26].

To evaluate Res-Cou6@NPs radiosensitizing potential, B16F10 melanoma cells were treated with IC_{50} concentrations of plain cisplatin, resveratrol & nanoparticles (Plain NPs, Res@NPs, Cou6@NPs, Res-Cou6@NPs) and exposed to 4 Gy at a dose rate of 0.8 Gy·min^{-1} for 5 min of radiation. Briefly, 1×10^4 cells/well were seeded in 96-well plates and incubated for 24 h at 37 °C in a 5% CO_2 atmosphere. Following treatment with IC_{50} nanoparticle concentrations, plates were incubated for 24 h prior to irradiation. Post-irradiation, cells were incubated for an additional 24 h before the addition of MTT reagent (5 mg/10mL, 3 h of incubation). Formazan crystals were solubilized with DMSO, and absorbance was recorded at 570/630 nm using a multi-mode plate reader (BIORAD Microplate Reader) [27].

3.7.3 Intracellular Uptake Analysis

Cellular uptake of Res-Cou6@NPs in B16F10 melanoma cells was evaluated using fluorescence microscopy. Cells (2×10^4) were seeded on coverslips in 24-well plates and incubated for 24 h. Following incubation, cells were treated with 22 µg/mL of Res-Cou6@NPs for 4 h at 37 °C, 5% CO_2. Cells were subsequently fixed with 4 % paraformaldehyde, permeabilized with 0.001% Triton X-100 (5 min), and counterstained with DAPI, nuclear stain (10 min) prior to fluorescence imaging in Zoe microscope [28].

3.7.4 Live/Dead Cell Staining Assay

The Live/Dead assay utilized FDA and PI to evaluate membrane integrity and metabolic activity in B16F10 melanoma cells. Cells (2×10^5/well) were seeded in 12-well plates and incubated for 24 h to facilitate adhesion. Subsequently, cells were administered with Res-Cou6@NPs (22 µg/mL), Res@NPs (39 µg/mL), and Cou6@NPs (52 µg/mL) for 24 h at 37 °C, followed by FDA/PI staining and imaging with a Zoe fluorescent microscope. To assess the impact of radiation, cells treated with

nanoparticles were irradiated with 4 Gy at a dose rate of 0.8 $Gy \cdot min^{-1}$ for 5 mins, incubated for 24 h, and subsequently stained with FDA/PI for imaging [29].

3.7.5 Dual Fluorescent Staining Assay

The anticancer mechanism of Res-Cou6@NPs was assessed via AO/EtBr dual labeling to distinguish live, apoptotic and necrotic cells. B16F10 melanoma cells (2×10^5/well) were cultured and treated with IC_{50} concentrations of Res@NPs, Cou6@NPs, and Res-Cou6@NPs for 24 h in 24-well plates. Cells were then stained with AO (10 µg/mL) and EtBr (10 µg/mL) in the dark for 20 min, washed to eliminate excess dye, and photographed using Zoe fluorescence microscopy to evaluate nuclear morphological alterations [30].

3.7.6 ROS Generation Study

ROS generation in nanoparticle-treated B16F10 melanoma cells was quantified using the DCFDA assay. This method detects oxidative stress through fluorescence emission upon interaction with ROS species, including hydrogen peroxide (H_2O_2), hydroxyl radicals ($^{\cdot}OH$), and peroxynitrite ($ONOO^-$)[31]. Cells (2×10^5/well) were seeded in 12-well plates, and treated with Res@NPs, Cou6@NPs, and Res-Cou6@NPs for 24 h. Post-treatment, cells were incubated with 10 µM DCFDA for 30 min at 37 °C and fluorescence was visualized microscopically (Zoe Microscope) and quantified via Image J software.

3.7.7 Singlet oxygen detection using SOS G

The term "SOS (Singlet Oxygen Species)" study typically refers to the investigation of singlet oxygen ($^1O_2$), a highly reactive form of ROS. It is an electronically excited state of molecular oxygen (O_2) that plays a major role in photodynamic therapy (PDT), oxidative stress, and cellular signaling [32]. The efficiency of singlet oxygen ($^1O_2$) generation by Res@NPs, Cou6@NPs, and Res-Cou6@NPs was assessed in real-time utilizing SOS G. In this experiment, B16F10 melanoma cells were seeded at a density of 2×10^5 cells/well in 12-well plates. Following a 24-hour incubation period, the cells were administered the corresponding nanoparticle formulations. Thereafter, SOS G dye was introduced to the treated cells, and fluorescence pictures were captured using a Zoe fluorescence microscope to assess singlet oxygen species generation.

3.7.8 Mitochondrial Membrane Potential Analysis

The variations in mitochondrial membrane potential ($\Delta\Psi m$) caused by Res@NPs, Cou6@NPs, and Res-Cou6@NPs in B16F10 melanoma cells were assessed using JC-1 staining. After 24 h of nanoparticle treatment, cells were treated with JC-1 dye (2 µM) at 37 °C for 30 minutes, washed with 1×PBS, and images were taken using fluorescence microscopy (Zoe Microscope). JC-1 exhibits potential-dependent spectral shifts: J-aggregates emit red fluorescence (~590 nm) in polarized (healthy) mitochondria, while J-monomers emit green fluorescence (~530 nm) in depolarized (apoptotic) mitochondria, enabling quantitative & qualitative assessment of mitochondrial membrane potential [33].

3.7.9 Cell Scratch Assay

Scratch assay was performed to analyze the antimetastatic properties of the Res-Cou6@NPs. Briefly, 5×10^4 B16F10 melanoma cells/well were seeded in a 24-well plate and incubated for 24 h in a CO_2 incubator. In each well a scratch was created and the cells were then treated with all the particles. Untreated cells were taken as a negative control [34]. The migration effect was analyzed under an Olympus fluorescence microscope at time intervals (0, 6, 12, 24, and 48 h). The percentage of scratch closure was calculated at each time interval compared to "t0".

3.7.10 Clonogenic Assay

A clonogenic assay was performed on B16F10 melanoma cells with slight modifications from the previously reported methods [35]. 2×10^5 B16F10 melanoma cells were seeded in a 24-well plate and incubated at 37 ^oC for 24 h. Following the incubation period, each group (Untreated, Plain NPs, Res@NPs, Cou6@NPs, and Res-Cou6@NPs) was assigned four wells for treatment. The cells were trypsinized on 4^{th} day of the incubation and were cultured on a 35 mm petri dish to analyze the regeneration of the remnant cells. The plates were washed with 1×PBS and maintained in fresh media for 7 days in a CO_2 incubator. After that, on the 7^{th} day, the developed colonies were thoroughly washed with 1×PBS, fixed with 4% paraformaldehyde, and visualized by staining with a 0.5% crystal violet dye [36,37].

3.7.11 3D Spheroid Formation Assay

B16F10 melanoma spheroids were formed via the hanging drop method by preparing a single-cell suspension at 1,000 cells/20 µL droplet. Droplets were applied to the inside surface of a petri dish lid (60-100 mm diameter), ensuring uniform spacing to avert coalescence. The lid was placed upside down over a humidification chamber filled with sterile 1×PBS to reduce evaporation. Following 72 h incubation (37 °C, 5% CO_2), gravity-driven cell aggregation yielded compact spheroids, which were harvested with wide-bore pipettes. Harvested spheroids were treated with NPs and incubated for 24 h [38,39]. FDA/PI dyes were used to stain the cells and imaging was done using a

Zoe Microscope.

3.7.12 Immunofluorescence

B16F10 melanoma cells were seeded in 96-well plates at a density of 1 × 10^3 cells/well. The cells were treated with nanoparticles and subsequently irradiated with 4 Gy's and incubated for 12 h, immunofluorescence staining was performed following the manufacturer's instructions. In brief, the cells were fixed for 15 min, followed by a 15-min blocking step, and then incubated with a rabbit monoclonal anti-γ-H2AX primary antibody for 1 hour at room temperature, after which Alexa Fluor-488-conjugated anti-rabbit secondary antibody was added for another hour under the same conditions and the cells were visualized using a Zoe fluorescence microscope [29].

3.7.13 Statistical Analysis

All experiments were performed with three separate biological replicates (n = 3), and the findings are expressed as the mean ± standard deviation (SD). Statistical evaluations were conducted utilizing one-way and two-way analysis of variance (ANOVA), with Tukey's post hoc test employed for multiple comparisons. Statistical significance was established as a p-value < 0.0001.

4. Results and Discussion

4.1. Synthesis and Characterization of Nanoparticles

The Res-Cou6@NPs were synthesized using the Solvent Evaporation Method. 0.5 mg/mL & 0.3 mg/mL concentration of Drug (Resveratrol) and Dye (Coumarin-6) in the ratio of 5:3 was loaded into the liposomes (Res-Cou6@NPs) at the time of synthesis. The prepared Res-Cou6@NPs were analyzed for UV-visible absorbance. The peaks at 307 and 458 nm indicate the presence of Res and Cou6, respectively, confirming their loading into the nanoparticles, as shown in Figure 2B. The standard curves of the Drug and Dye were plotted, and the regression coefficients were found to be 0.9988 and 0.9975, respectively (Figures S1e and f). The drug and dye encapsulation efficiency (EE%) was calculated based on the dose-response curve. The EE% of the drug in Res@NPs was found to be 60% and in Res-Cou6@NPs was 85% and dye's EE% was found to be 80% in Cou6@NPs and 90% in Res-Cou6@NPs, as shown in Figure 2G. It is observed that the EE% of the drug and dye increased in the main particle (Res-Cou6@NPs) due to interaction of the drug and dye. The possible reasons for this could be synergistic interactions between molecules (such as a drug and dye interacting via hydrogen bonding, π-π stacking, or hydrophobic interactions), leading to a more stable complex that is better retained within the nanoparticle. One compound may improve the solubility or compatibility of the other in the carrier matrix, enhancing overall encapsulation [40,41]. Structures of all the compounds (Res, Cou 6, and Soya PC) are represented in Scheme 2. The bright field and UV images of all the particles (Res@NPs, Cou6@NPs, and Res-Cou6@NPs) are shown in Figure 2A. Fluorescence spectroscopy characterized Resveratrol ($\lambda_{ex}/\lambda_{em}$ = 362/406 nm) and Coumarin-6 ($\lambda_{ex}/\lambda_{em}$ = 457/501 nm) in NPs (Figures 2c, S2m-p). Solvent dependent spectral profiles of Res and Cou6 are detailed in Figures S1b-d and S2a-l. To overcome the inherent aqueous insolubility of the plain drug and dye (Figure S1a), the nanoformulation significantly enhanced dispersion, enabling the biological application of the compounds. DLS revealed hydrodynamic diameters of 116.93 ± 0.2 nm (Plain NPs), 177.76 ± 1.2 nm (Res@NPs), 182.95 ± 3.2 nm (Cou6@NPs), and 195.77 ± 2.2 nm (Res-Cou6@NPs) (Figures 1A-D, Table 1). Zeta potentials measured -0.50 ± 0.2 mV (Plain NPs), -4.50 ± 1.2 mV (Res@NPs), -6.20 ± 1.0 mV (Cou6@NPs), and -30 ± 2.2 mV (Res-Cou6@NPs) (Figure 1E). The significant decrease to -30 mV for co-loaded nanoparticles indicates surface charge modulation, likely due to compositional reorganization that exposes anionic groups, thereby enhancing colloidal stability through electrostatic repulsion. PDI were 0.319 (Plain NPs), 0.129 (Res@NPs), 0.175 (Cou6@NPs), and 0.233 (Res-Cou6@NPs), corroborated by SEM confirming monodispersity and uniform morphology (Figure 1F, Table 1).

Table 1. Hydrodynamic size, PDI, and zeta potential of all synthesized nanoparticles.

NPs	Hydrodynamic Size (nm)	PDI	Zeta Potential (mV)
Plain NPs	116.93 ± 0.2	0.319	-0.50 ± 0.2
Res@NPs	177.76 ± 1.2	0.129	-4.50 ± 1.2
Cou6@NPs	182.95 ± 3.2	0.179	-6.20 ± 1.0
Res-Cou6@NPs	195.77 ± 2.2	0.233	-30 ± 2.2

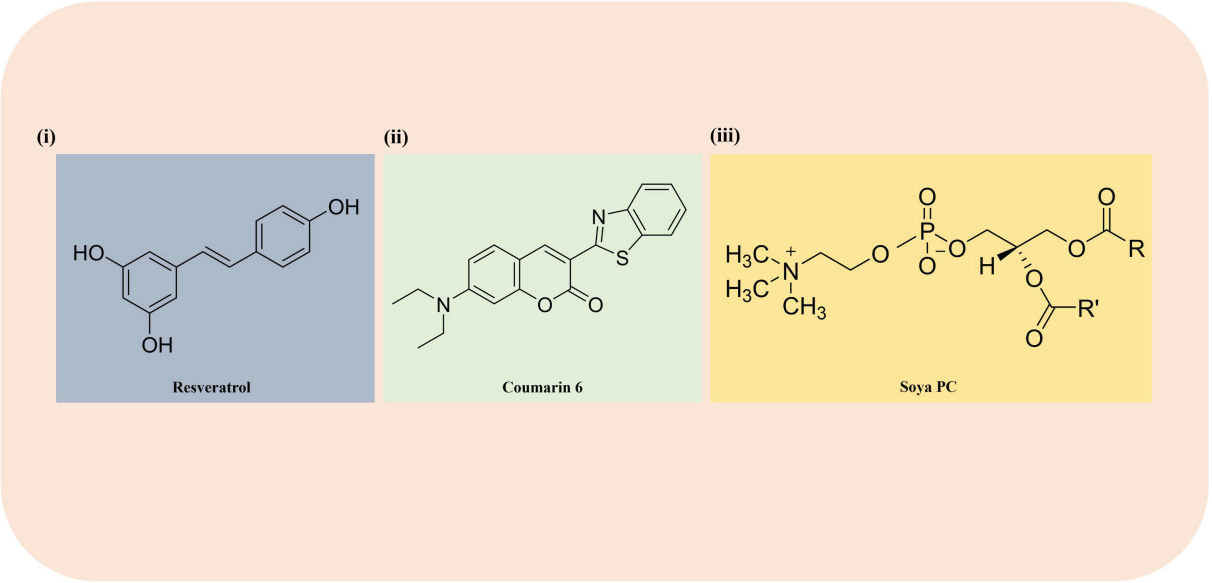
The hydrodynamic diameter of our Res-Cou6@NPs was measured to be around 200 nm, a size range generally regarded as ideal for extended blood circulation and efficient tumor localization through the enhanced permeability and retention (EPR) effect, which is often observed in solid tumors, including certain melanoma regions [42]. The key determinant of the *in vivo* performance and therapeutic success of intravenously delivered nanoparticles is their physiochemical characteristics, i.e.; particle size. Upon entering the bloodstream, nanoparticles must

surmount multiple biological obstacles, including dodging swift pickup by the reticuloendothelial system (RES) in organs such as the liver and spleen, and effectively navigating the permeable vasculature of tumors to reach the tumor microenvironment [43]. Nanoparticles smaller than 10 nm are often rapidly excreted through renal filtration, but those larger than 200 nm are more susceptible to sequestration by the RES. Due to the heterogenous characteristics of the EPR effect in melanoma, resulting from its rich extracellular matrix and uneven vasculature, it is essential to maintain an ideal nanoparticle size to ensure maximum accumulation and deep tissue penetration after systemic or local delivery. In addition to particle size, surface charge significantly influences nanoparticle stability, cellular interactions, and biological efficacy. The significant alteration in zeta potential to around −30 mV in the co-loaded nanoparticles indicates modifications in surface composition and the exposure of negatively charged functional groups. This heightened negative surface charge can enhance electrostatic repulsion among nanoparticles, diminishing aggregation and augmenting colloidal stability. As a result, the improved stability could facilitate more uniform nanoparticle distribution and possibly boost their engagement with cells [44,45].

4.2 XRD and FTIR Studies of Nanoparticles

FTIR analysis was performed to ascertain the functional group present in the synthesized Res-Cou6@NPs (Figure 2E). This approach elucidates the interactions between the drug, lipid, and dye, which may influence the release patterns of the drug or dye. The FTIR spectrum displays a distinct peak at 1608 cm^{-1} in pure Res, indicative of robust aromatic C-C double bond stretching, which is similarly observed in Res-Cou6@NPs. In Soya Pc, a characteristic absorption band is observed at 1739 cm^{-1}, corresponding to C=O bonds; 2850 cm^{-1} is associated with symmetric stretching, whereas 2920-2950 cm^{-1} pertains to asymmetric stretching. The peak at 1735 cm^{-1} corresponds to C=O stretching vibration of Cou6. A notable band at approximately 1620 cm^{-1} suggests the existence of C=C bonds. The broadband about 3300 cm^{-1} is likely due to interactions among the drug, dye, and lipid constituents [46]. Consequently, FTIR analysis verifies the existence of many functional groups, including -OH, -CH, and -NH_2, from Res, Cou6, and Soya PC in the synthesized Res-Cou6@NPs.

XRD examination (Figure 2D) analyzed the crystalline structures of pure Res, Cou6, Soya PC, and Res-Cou6@NPs. Pure Res and Cou6 displayed distinct diffraction peaks, affirming their crystallinity. The Soya PC exhibited a comparable amorphous halo at 2θ around 20^0-25^0. The co-loaded nanoparticles exhibited a comparable amorphous halo devoid of crystalline drug peaks, signifying molecular dispersion inside the lipid bilayer. The reduction in crystallinity verifies the amorphization of the drug during encapsulation, a change that improves the solubility and bioavailability of both drug and dye [47,48].



Scheme 2. Chemical structure of (i) Resveratrol, (ii) Coumarin 6, and (iii) Soya PC.

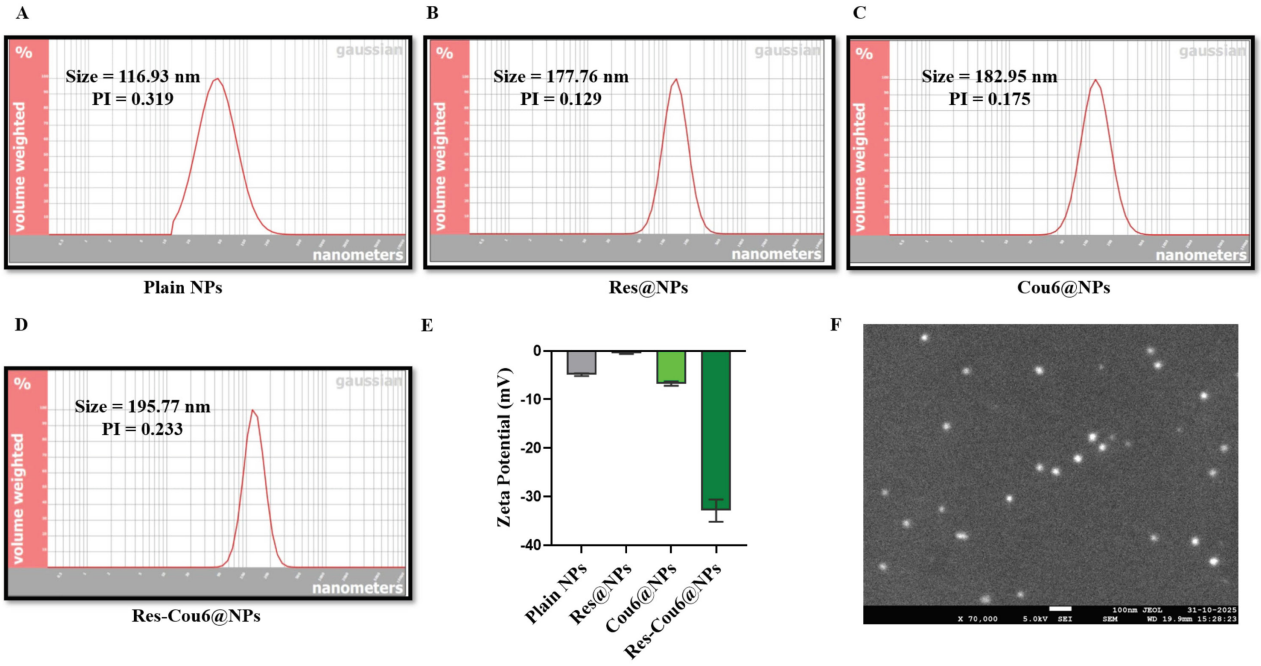


Figure 1. Characterization of NPs. (A-D) DLS analysis illustrating the particle size distribution characteristics of (A) Plain NPs, (B) Res@NPs, (C) Cou6@NPs, and (D) Res-Cou6@NPs. The plots depict the distribution of hydrodynamic diameters for each nanoparticle formulation assessed via DLS, showing the mean particle size and size distribution after the encapsulation of Res, and Cou6. (E) Zeta potential assessments of Plain NPs, Res@NPs, Cou6@NPs, and Res-Cou6@NPs, illustrating the surface charge and colloidal stability of various nanoparticle formulations. (F) SEM image of Res-Cou6@NPs illustrating the structure and surface features of the produced nanoparticles.

Figure 2I shows how Res-Cou6@NPs release drugs *in vitro* over 48 h in both basic and acidic environments. The release behavior is noticeably different, which shows that the nanoformulation is pH-responsive. Under the basic conditions, the nanoparticles show a very fast augmented drug release, with almost all of the drug being released in the first 12-16 hours, and then the release slows down with time. On the other hand, drug release is limited and stays the same at acidic pH for the same amount of time [49,50]. This distinct release pattern shows that Res-Cou6@NPs are more stable under acidic circumstances, such the tumor microenvironment or intracellular endosomal compartments. This stops drugs from leaking out too soon when they are circulating. The higher release at neutral pH indicates that the formulation can provide controlled and environmentally sensitive drug delivery, enhance therapeutic efficacy at targeted sites, and minimize systemic side effects. The pH-dependent release properties show that Res-Cou6@NPs could be a complex delivery system that responds to stimuli to improve the bioavailability and therapeutic effectiveness of Resveratrol in cancer treatment [51–53].

To assess the stability of the synthesized nanoformulation, nanoparticles were stored at -4 °C in the dark for 30 days in both water and PBS, with hydrodynamic size and PDI measured at 7-day intervals (Figure 2F). Res-Cou6@NPs demonstrated no significant changes in size or PDI over the 30-day storage period, indicating excellent colloidal stability [54].

Following physicochemical validation, the radiosensitizing performance of the nanoplatform was evaluated under biologically stringent conditions.

4.3 Radiosensitization in *Deinococcus radiodurans*

To establish a stringent evaluation of radiosensitization capability, we first investigated the performance of Res-Cou6@NPs in the extreme radioresistant bacterium *Deinococcus radiodurans*.

4.3.1 Bacterial Clonogenic Survival Assay

The biocompatibility concentration of Res-Cou6@NPs was found to be 100 µg/mL on NIH 3/T3 and L929 cell lines, therefore the concentration within the biocompatibility range, 100 µg/mL is used for the radiosensitization study. The overnight incubated MH Agar plates with the spot revealed the significant difference in the number of colonies and the size of the spot. As shown in Figure 3a, and S3b, the Res-Cou6@NPs treated sample showed lower number of colonies at 10^{-12} dilution when compared to other control groups. Similarly, the X-Ray irradiated group of Res-Cou6@NPs showed further reduced number of colonies and size, in the spot when compared to non-irradiated group.

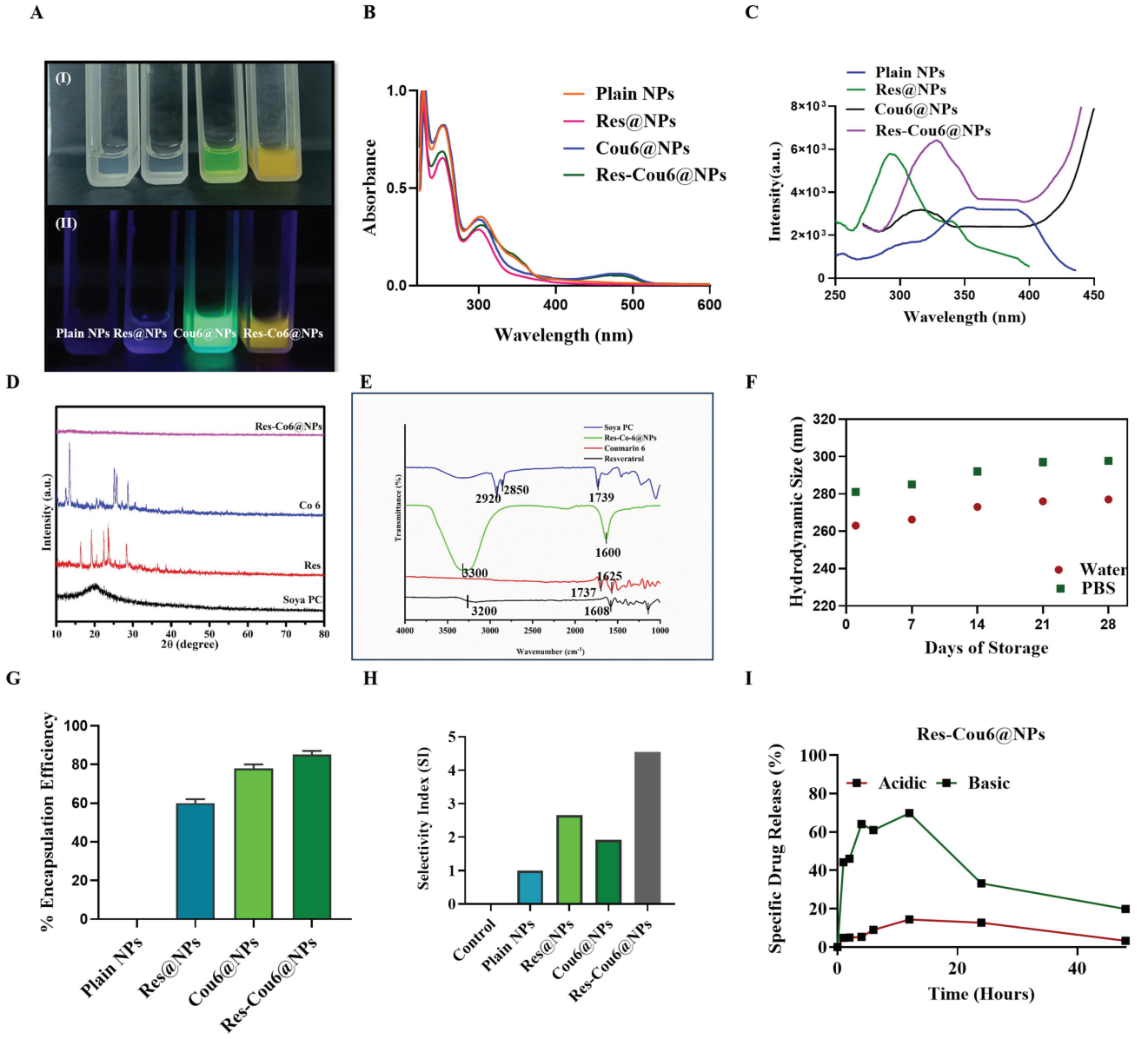


Figure 2. (A) Images captured under bright-field and UV illumination of Plain NPs, Res@NPs, Cou6@NPs, and Res-Cou6@NPs, showing the visual picture and fluorescence of the formulations. (B) UV-Vis absorption spectra of Plain NPs, Res@NPs, Cou6@NPs, and Res-Cou6@NPs validate the effective encapsulation of Resveratrol and Coumarin-6. (C) Fluorescence emission spectra of Plain NPs, Res@NPs, Cou6@NPs, and Res-Cou6@NPs illustrating the fluorescence properties of Coumarin-6 post-encapsulation. (D) XRD patterns of Soya PC, Resveratrol, Coumarin-6, and Res-Cou6@NPs exhibit the crystalline properties of the constituents and the formulation. (E) FTIR spectra of Soya PC, Resveratrol, Coumarin-6, and Res-Cou6@NPs validate the presence of distinctive functional groups and the encapsulation of the drug and dye. (F) The stability of Res-Cou6@NPs in aqueous solutions and PBS over the duration of the investigation. (G) The encapsulation efficiency (%) of Res@NPs, Cou6@NPs, and Res-Cou6@NPs. (H) Selectivity index of Plain NPs, Res@NPs, Cou6@NPs, and Res-Cou6@NPs. (I) The *in vitro* drug release of Res-Cou6@NPs at both physiological and acidic pH levels.

The results in the colony forming Assay also exhibited the similar results. As shown in Figure 3b, and S3a it was observed that Res-Cou6@NPs inhibited colony formation in *Deinococcus radiodurans*. The effect of Res-Cou6@NPs was enhanced when combined with X-Ray irradiation, which is evident from the fewer colonies formed when compared with other controls. Thus, Res-Cou6@NPs in combination with X-Ray irradiation could potentially be used as a radiosensitizing nanoformulation. Raw plate images of spots were shown in Figure S6 & 7.

4.3.2 Radiation-Induced Bacterial Cell Damage Assay

The SYTO9-PI staining determined the live and dead cells. The X-Rays irradiated and non-irradiated bacterial cells were stained with SYTO9 and PI to determine the cell viability. The X-Ray irradiated group exhibited more red fluorescence, which indicated bacterial cell death. The non-irradiated control groups showed more green fluorescence, representing more viable/live cells (Figure 3c & S4,5). This demonstrated the efficacy of Res-Cou6@NPs in combination with X-Ray irradiation for inhibiting

bacterial growth suggesting radiosensitizing potential of Res-Coui6@NPs.

The observed radiosensitization is particularly notable given the extreme intrinsic radioresistance of *Deinococcus radiodurans*, sustained by highly efficient DNA repair, robust antioxidant defenses, and protein protection systems. Treatment with Res-Cou6@NPs resulted in a marked reduction in post-irradiation reproductive viability, indicating effective disruption of bacterial radioresistance under ionizing radiation. Complementary membrane integrity assays revealed pronounced early cellular damage, suggesting that radiosensitization is mediated through acute structural impairment rather than solely delayed growth inhibition. The strong correlation between immediate membrane damage and long-term survival loss supports a mechanism involving rapid compromise of cellular defense pathways.

Importantly, these findings establish a mechanistic basis that parallels resistance phenomena observed in radioresistant cancer cells, including melanoma. Building on this validated extreme-resistance model, subsequent mammalian studies were designed to examine whether the radiosensitization trends observed in *Deinococcus radiodurans* translate to tumor-relevant systems.

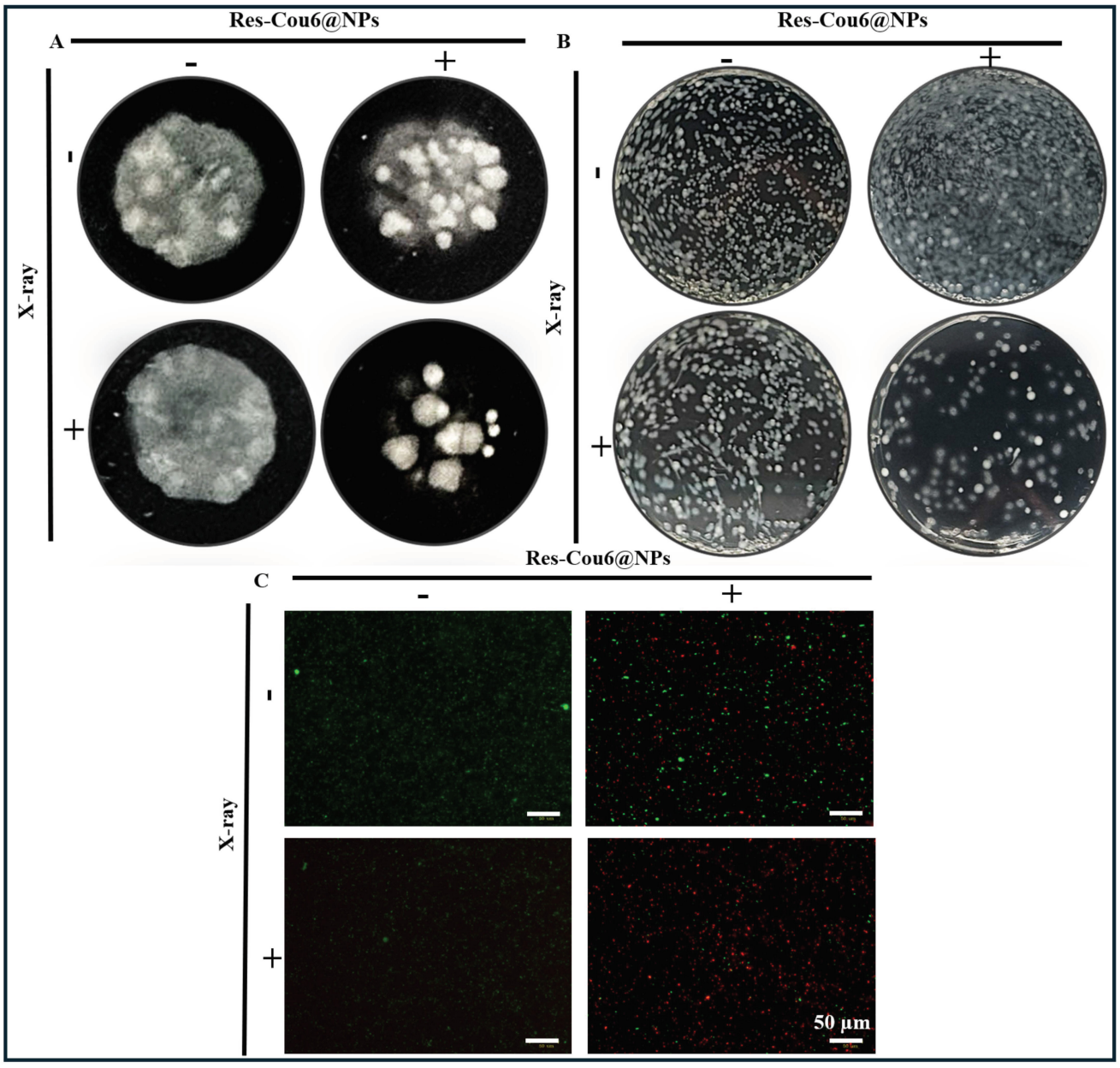


Figure 3. Evaluation of the radiosensitizing effect of Res-Cou6@NPs on *Deinococcus radiodurans*. (A) Spot assay demonstrating the viability of *Deinococcus radiodurans* after exposure to Res-Cou6@NPs with and without radiation. (B) Spread assay demonstrating the growth of bacterial colonies under various treatment conditions. (C) Live/Dead fluorescence experiment demonstrating bacterial viability post-treatment with Res-Cou6@NPs, both with and without radiation.

The application of *Deinococcus radiodurans* in this study was designed as a rigorous biological model to assess the inherent radiosensitizing capabilities of the synthesized nanoplatform, rather than to determine a direct quantitative relationship with mammalian tumor models. Due to its remarkable resilience to ionizing radiation and oxidative stress, *Deinococcus radiodurans* serves as an effective model for evaluating if the formulation may surpass essential cellular defense mechanisms linked to radioresistance. Although the molecular pathways that regulate radiation response vary significantly between prokaryotic and mammalian cells, the bacterial model acts as a preliminary resistance-screening tool to assess the impairment of conserved stress-protective mechanisms, especially in the context of oxidative stress management and DNA damage tolerance. The ensuing confirmation of the nanoplatform in mammalian melanoma cells offers biological proof that the identified radiosensitizing effects extend beyond the bacterial model, thereby enhancing the translational significance of the results. Nonetheless, this cross-kingdom assessment ought to be regarded as a supplementary approach rather than a definitive forecast of clinical treatment results, necessitating additional confirmation via *in vivo* research.

4.4 Cell Viability Studies

Biocompatibility of the synthesized nanoparticles (Plain NPs, Res@NPs, Cou6@NPs, and Res-Cou6@NPs) were evaluated using an MTT assay in L929 and NIH3/T3 cell lines. The cells were treated with the experimental groups at concentrations (1, 2.5, 5, 10, 25, 50, and 100 µg/mL) along with the untreated controls and incubated for 24 h. The cells exhibited more than 80% cell viability at the concentration of 50 µg/mL for Res@NPs and Res-Cou6@NPs.

For Plain NPs & Cou6@NPs the concentration is 100 µg/mL, representing compatibility of the synthesized liposomes on normal cell lines, as shown in Figure 4A, B. (Bar graph of the same shown in the S8a, b).

The cytotoxicity was analyzed using an MTT assay on different type of cancer cells: B16F10 melanoma cells, HeLa cervical cancer cells, and 4T1 breast cancer cells. Briefly, the cells were treated with the experimental groups at the same concentration as biocompatibility, along with the untreated controls, and incubated for 24 h. The 50% cell death of Res-Cou6@NPs in HeLa was achieved at 100 µg/mL, in 4T1 at 80 µg/mL, and in B16F10 melanoma cells at 22 µg/mL. In B16F10 melanoma cells, Res@NPs and Cou6@NPs exhibited IC_{50} values of 39 µg/mL and 52 µg/mL, respectively. On the other hand, Cou6@NPs needed 86 µg/mL to kill half of the 4T1 breast cancer cells. These results are showing that the nanoformulation works better on melanoma cells than on breast cancer and cervical cancer models (Figures 4C-E; S8c-e), which shows that it works best on melanoma.

Comparative research indicates that nanocarrier systems have enhanced therapeutic characteristics compared to conventional medicines via various mechanisms. This encompasses improved medication solubility and bioavailability, targeted delivery to diseased areas, and safeguarding against enzymatic degradation. Nanocarriers enhance controlled release kinetics, promote more cellular internalization, and diminish systemic toxicity by limiting off-target exposure. They enable combinatorial delivery of therapeutic drugs and facilitate surface functionalization with active targeting ligands, positioning them as a versatile platform for improved drug delivery applications [55–57].

The radiation-induced cytotoxicity was evaluated by an MTT test on B16F10 melanoma cells. The cells were subjected to 4 Gy at a dosage rate of 0.8 Gy min^{-1} for 5 minutes following treatment with IC_{50} values of all particles (Plain NPs, Res@NPs, Cou6@NPs, and Res-Cou6@NPs) as well as plain Resveratrol and Cisplatin, and were subsequently incubated for 3 hours at 37 °C. The radiation-mediated Res-Cou6@NPs exhibited a cell viability of 40±0.1% relative to other treatment groups, indicating a reduction in cell proliferation (Figure 8C). In the radiation groups, cell viability was decreased relative to control group.

The Selectivity Index (SI) is an essential quantitative measure for assessing the differential cytotoxicity of medicinal drugs, such as Resveratrol and Coumarin-6, towards diseased and healthy cells. This metric is crucial in preclinical drug development, especially in oncology, parasitology, and diagnostic imaging, where selective targeting reduces off-target toxicity and improves therapeutic windows. SI values exceeding 1 signify advantageous selectivity, with elevated values associated with enhanced clinical translation potential.

$$SI = IC_{50}(\text{normal cells})/IC_{50}\ (\text{target/diseased cells})$$

The SI analysis demonstrated varying targeting efficacy: plain NPs (SI ≈ 1), Res@NPs (SI = 2.66), Cou6@NPs (SI = 1.92), and Res-Cou6@NPs (SI = 4.54). Res-Cou6@NPs exhibited markedly improved selectivity (SI = 4.54), signifying a superior preference for malignant cells compared to healthy ones. Cell line-specific SI values for Res-Cou6@NPs across HeLa, 4T1, and B16F10 melanoma models are comprehensively detailed in Table S1.

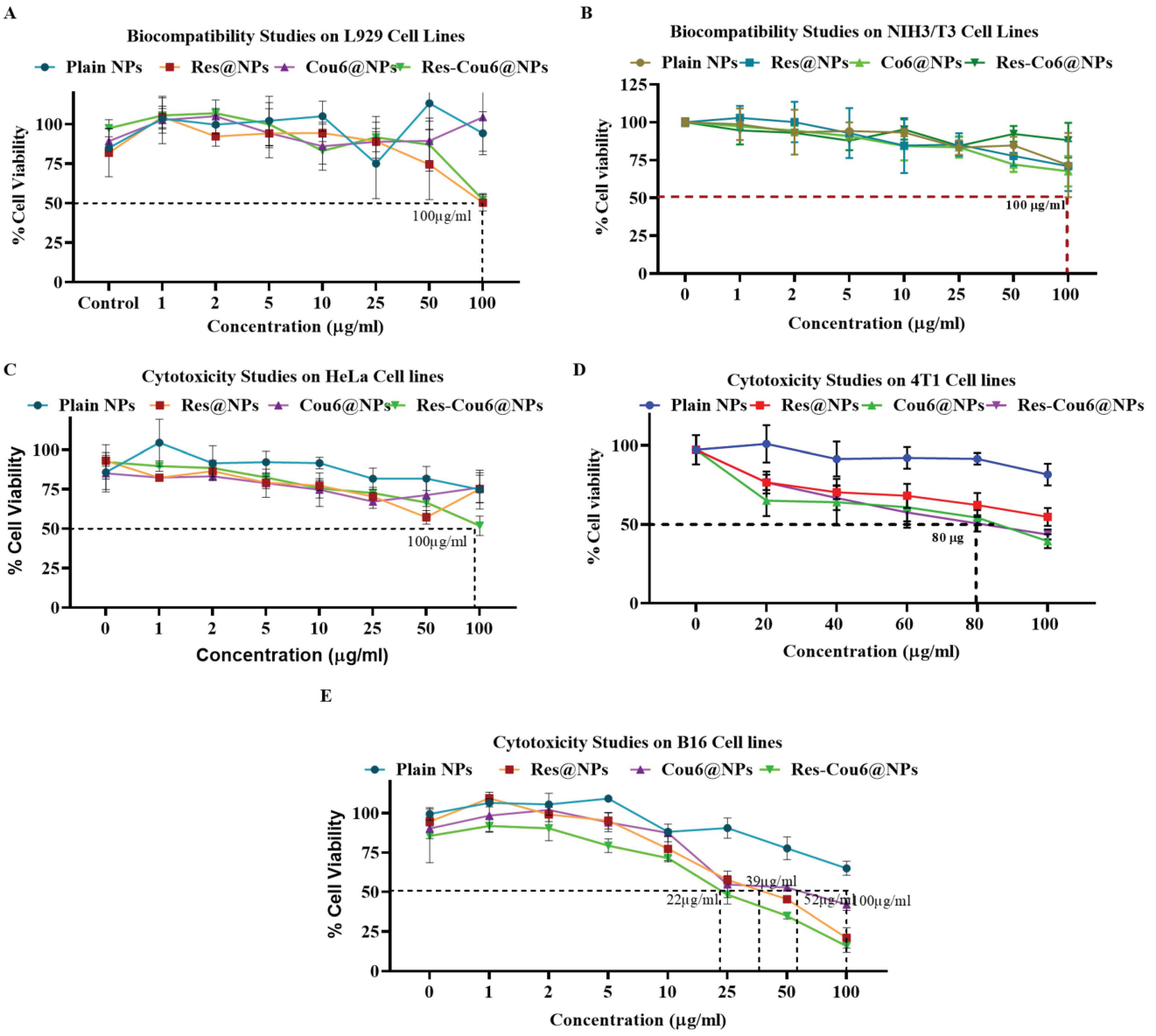


Figure 4. (A-B) Viability of normal cells post-treatment with Plain NPs, Res@NPs, Cou6@NPs, and Res-Cou6@NPs, illustrating the formulations' biocompatibility in (A) L929 and (B) NIH/3T3 cells. (C-E) Cytotoxicity study of Plain NPs, Res@NPs, Cou6@NPs, and Res-Cou6@NPs in dose-dependent manner (C) HeLa, (D) 4T1, and (E) B16F10 melanoma cells, demonstrating the anticancer efficacy of the various nanoparticle formulations.

The Combination Index (CI) quantitatively measures the interaction between two agents based on their effect on biological system (e. g; cell viability, apoptosis).

The formula to calculate CI is:

$$CI = \frac{(D_1)}{(D_{x1})} + \frac{(D_2)}{(D_{x2})}$$

Where:

- D_1 = IC_{50} of Resveratrol in Res-Cou6@NPs
- D_2 = IC_{50} of Coumarin 6 in Res-Cou6@NPs
- D_{x1} = IC_{50} of Resveratrol in Res@NPs
- D_{x2} = IC_{50} of Coumarin 6 in Cou6@NPs

According to the cell viability experiment, the CI value is 0.98, suggesting the synergistic effect of the nanoformulation [58,59].

4.5 Intracellular Uptake Analysis

Cellular internalization of Res-Cou6@NPs by B16F10 melanoma cell line was evaluated. Hydrophobic compounds (Resveratrol and Coumarin-6) exhibit inherently low cellular uptake, preventing them from reaching therapeutically effective intracellular concentrations. Optimal drug hydrophilicity is crucial for attaining both elevated cellular internalization and therapeutic effectiveness. Liposomal nanoparticles were synthesized to overcome this constraint by encapsulating hydrophobic chemicals within lipid bilayer structures.

Nile red was co-encapsulated into the Res-Cou6@NPs as a fluorescent marker for quantifying uptake. Cellular nuclei were counterstained with DAPI. The intrinsic green fluorescence of Coumarin-6 (Figure 5A, B, and S9a) has exhibited, suggesting the internalization of Cou6 in the cells.

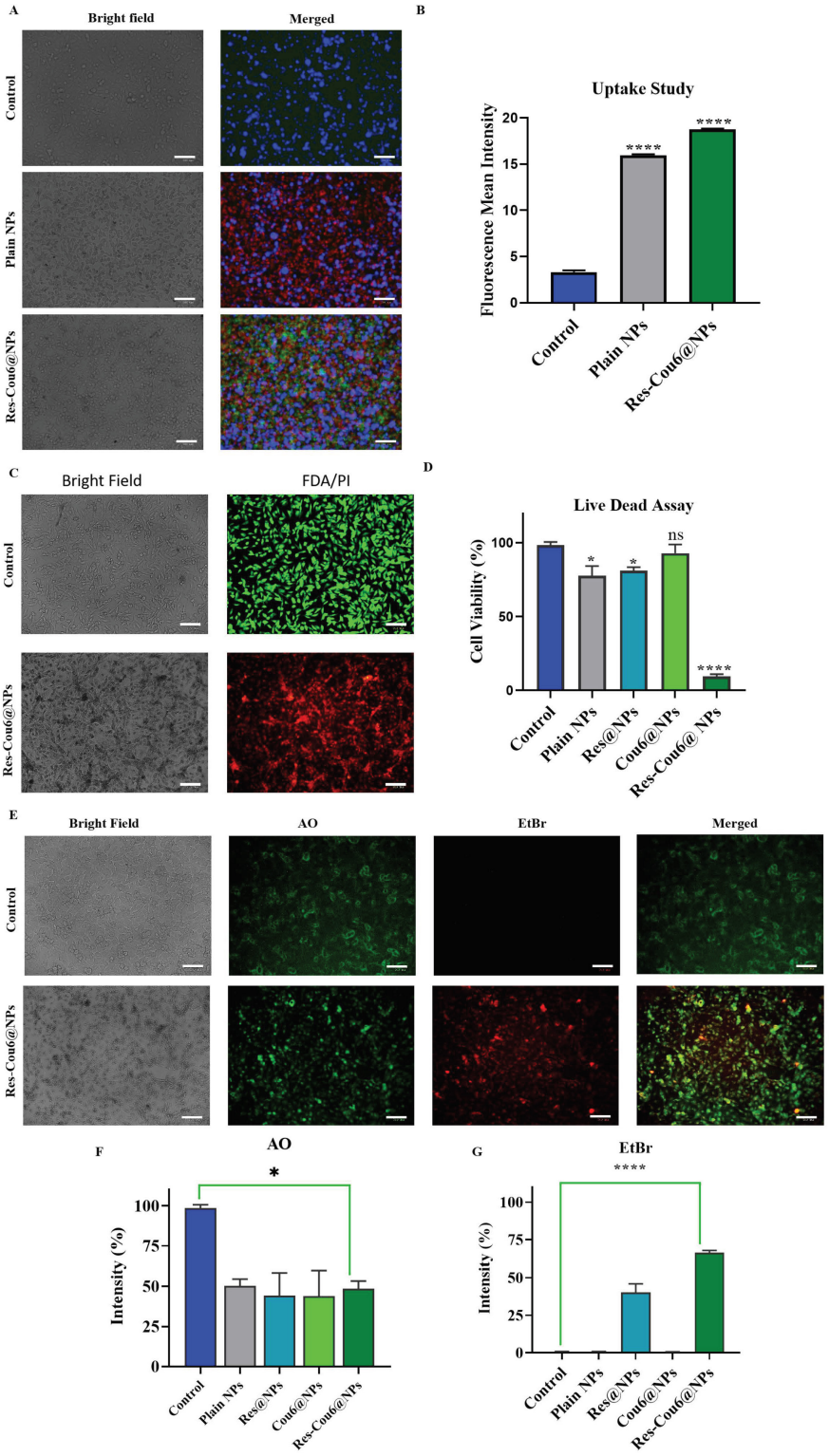


Figure 5. (A) Cellular uptake of Res-Cou6@NPs in B16F10 melanoma cells using Nile Red as a tracker dye (scale bar: 100 μm) (B) Quantification analysis for intracellular uptake of Res-Cou6@NPs (C) Live/Dead assay in B16F10 melanoma cells after treatment with Res-Cou6@NPs (scale bar: 100 μm) (D) Quantification analysis for Live/Dead assay of Plain NPs, Res@NPs, Cou6@NPs, and Res-Cou6@NPs (E) *In vitro* apoptosis evaluation in B16F10 melanoma cells by AO/EtBr staining after treatment with Res-Cou6@NPs (scale bar: 100 μm) (F, G) Quantification analysis for AO/EtBr assay of Plain NPs, Res@NPs, Cou6@NPs, and Res-Cou6@NPs. Data are presented as mean ± SD (n = 3 independent biological replicates).

4.6 Live/Dead Cell Staining Assay

The qualitative evaluation of produced liposome was conducted using a Live/Dead assay, employing FDA and PI staining to distinguish viable from non-viable cells. Figures 5C, D, and S10b display representative fluorescence micrographs. Following radiation-mediated analysis, utilizing the identical test methods, demonstrated analogous cellular responses, as illustrated in Figures 8A, B, and D, E, together with internal group images (Figure S12a: with radiation; Figure S12b: without radiation). Additional FDA/PI channel-separated images for Res-Cou6@NPs are provided in Figures S12c, d. Critically, the results demonstrate significantly elevated cellular mortality under irradiated conditions relative to non-irradiated controls.

4.7 Dual Fluorescent Staining Assay

To elucidate the mechanism of Res-Cou6@NPs-induced cytotoxicity, AO/EtBr dual staining was employed. This assay qualitatively distinguishes apoptotic cells through differential fluorescence: AO stains all cells green, while EtBr selectively permeates membrane-compromised apoptotic cells, emitting red fluorescence. Results demonstrated significant apoptosis induction in Res-Cou6@NPs-treated cells after 24 h, characterized by yellow-green fluorescence, relative to untreated controls (Figures 5E-G, and S10d) [60].

4.8 ROS Generation Study

The ability of the nanoformulation to induce ROS generation in B16F10 melanoma cells was assessed using the DCFDA assay. Following 24 h treatment with Plain NPs, Res@NPs, Cou6@NPs, or Res-Cou6@NPs, qualitative & quantitative analysis revealed substantial ROS induction in Res@NPs, Cou6@NPs, and Res-Cou6@NPs-treated cohorts (Figures 6A, B, and S9c). Resveratrol monotherapy also demonstrated considerable ROS generation, consistent with established mechanisms of Resveratrol-induced oxidative stress in malignant cells. Crucially, Res-Cou6@NPs exhibited significantly enhanced ROS production relative to controls, indicating synergistic ROS-mediated cytotoxicity. This work presents the initial evidence of Cou 6's inherent potential to induce ROS [61–63].

4.9 Singlet oxygen species generation detection using SOS G

The efficiency of singlet oxygen ($^1O_2$) generation for Plain NPs, Res@NPs, Cou6@NPs, and Res-Cou6@NPs was evaluated in real time utilizing SOS G. Green fluorescence, a sign of SOS G activation, was seen in the Res@NPs, Cou6@NPs, and Res-Cou6@NPs treatment groups via fluorescence microscopy, indicating the generation of singlet oxygen ($^1O_2$) (Figures 6C, D, and S9b). Quantitative examination of green fluorescence intensity was conducted utilizing Image J software. Res-Cou6@NPs demonstrated an elevated generation of singlet oxygen ($^1O_2$) relative to the control groups.

4.10 Mitochondrial Membrane Potential Analysis

ROS-induced mitochondrial dysfunction is a recognized mechanism that disturbs cellular homeostasis, ultimately initiating apoptotic cell death. JC 1 experiment was performed to evaluate mitochondrial damage induced by nanoparticles. This assay utilizes the potential-dependent accumulation of JC 1 in mitochondria: undamaged membranes facilitate JC aggregate formation (red fluorescence), whereas membrane depolarization results in monomeric JC 1 (green fluorescence). The results indicated significant increase in mitochondrial damage in cells treated with Res-Cou6@NPs compared to those treated with Plain NPs, Res@NPs, and Cou6@NPs after 24 h of exposure (Figures 6E-G, and S10a). Notably, Res@NPs and Cou6@NPs also induced substantial mitochondrial dysfunction, consistent with their established capacity to generate ROS. These findings confirm the nanoformulation's ability to selectively target mitochondria, the central organelles for cellular energy production, to initiate cytotoxic pathways [64–67].

4.11 Cell Scratch Assay

In multicellular organisms, cell migration represents a fundamental process that underpins gastrulation, neural development, tissue regeneration, and morphological adaptations, thereby facilitating tissue integration. Conversely, dysregulated migratory behavior under pathological conditions denotes *cell invasion*, characterized by aberrant infiltration into adjacent tissues. Malignant cells demonstrate significant invasive capacities, allowing them to infiltrate tissues and spread throughout the body, a phenomenon referred to as *metastasis*. Melanoma demonstrates this tendency, as initial tumor cells disseminate too far anatomical locations [68,69].

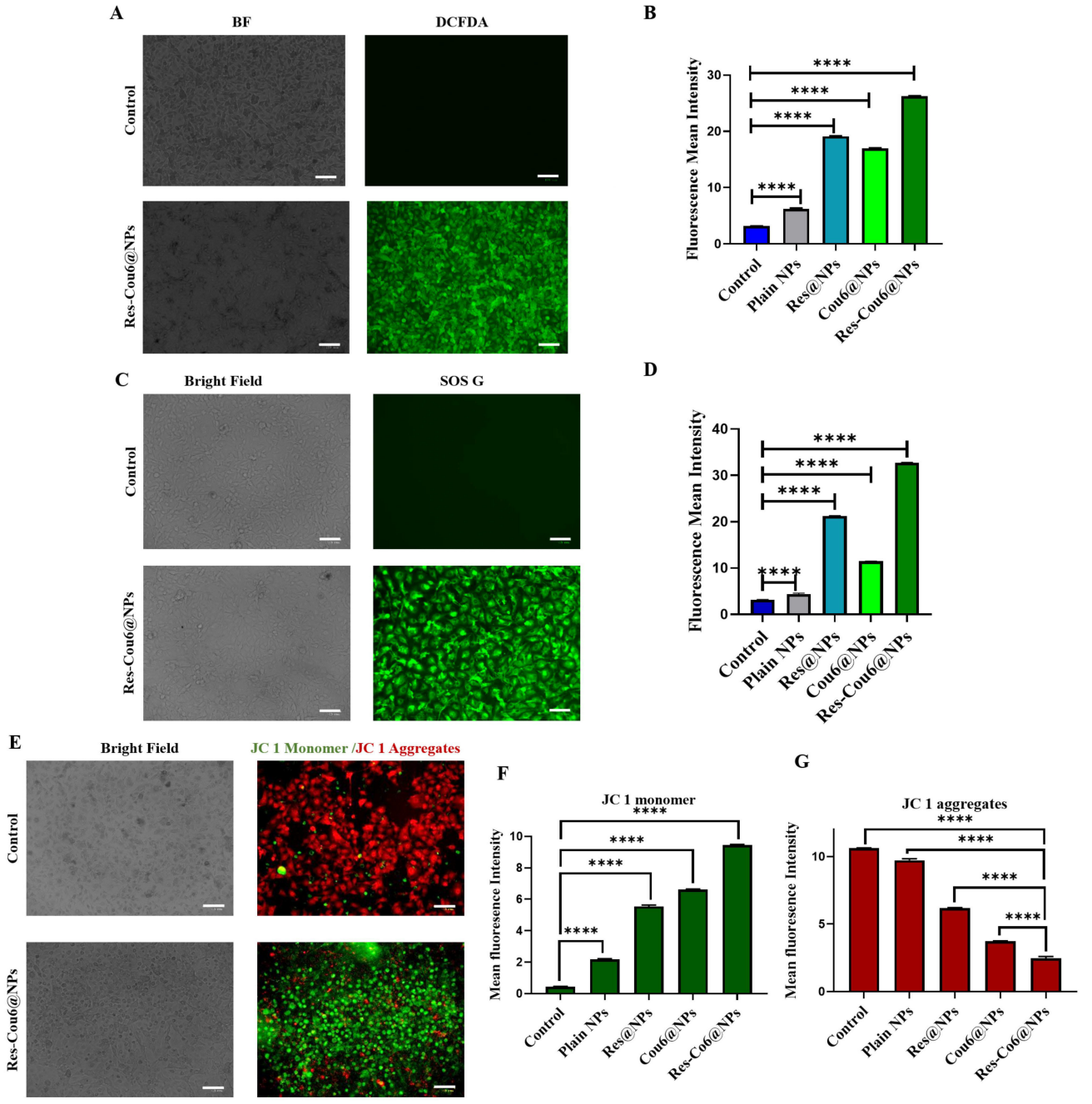


Figure 6. (A) ROS generation evaluation in melanoma cells after treatment with Res-Cou6@NPs by a DCFDA assay (scale bar: 100 μm) (B) Quantification analysis for DCFDA assay of Plain NPs, Res@NPs, Cou6@NPs, and Res-Cou6@NPs (C) Singlet oxygen species analysis of Res-Cou6@NPs by SOS G assay (scale bar: 100 μm) (D) Quantification analysis for SOS G assay of Plain NPs, Res@NPs, Cou6@NPs, and Res-Cou6@NPs (E) Mitochondrial damage evaluation by JC-1 staining in melanoma cells after treatment with Res-Cou6@NPs (scale bar: 100 μm) (F, G) Quantification analysis for JC-1 assay of Plain NPs, Res@NPs, Cou6@NPs, and Res-Cou6@NPs. Data are presented as mean ± SD (n = 3 independent biological replicates).

The anti-migratory effectiveness of Res-Cou6@NPs was assessed by a scratch-wound assay in densely packed cell monolayers. Control groups demonstrated substantial wound closure, while Res-Cou6@NPs therapy markedly inhibited cellular migration, resulting in nearly total suppression of scratch repopulation. Time-lapse imaging at 0, 6, 12, and 24 h confirmed sustained inhibitory effects (Figures 7A and S11). Quantitative analysis indicated less than 10% wound closure in treated wells compared to controls, suggesting statistically significant inhibition ($p < 0.0001$; Figure 7C). The finding demonstrates that Res-Cou6@NPs significantly hinder cancer cell motility, underscoring their potential as anti-metastatic nanoformulations.

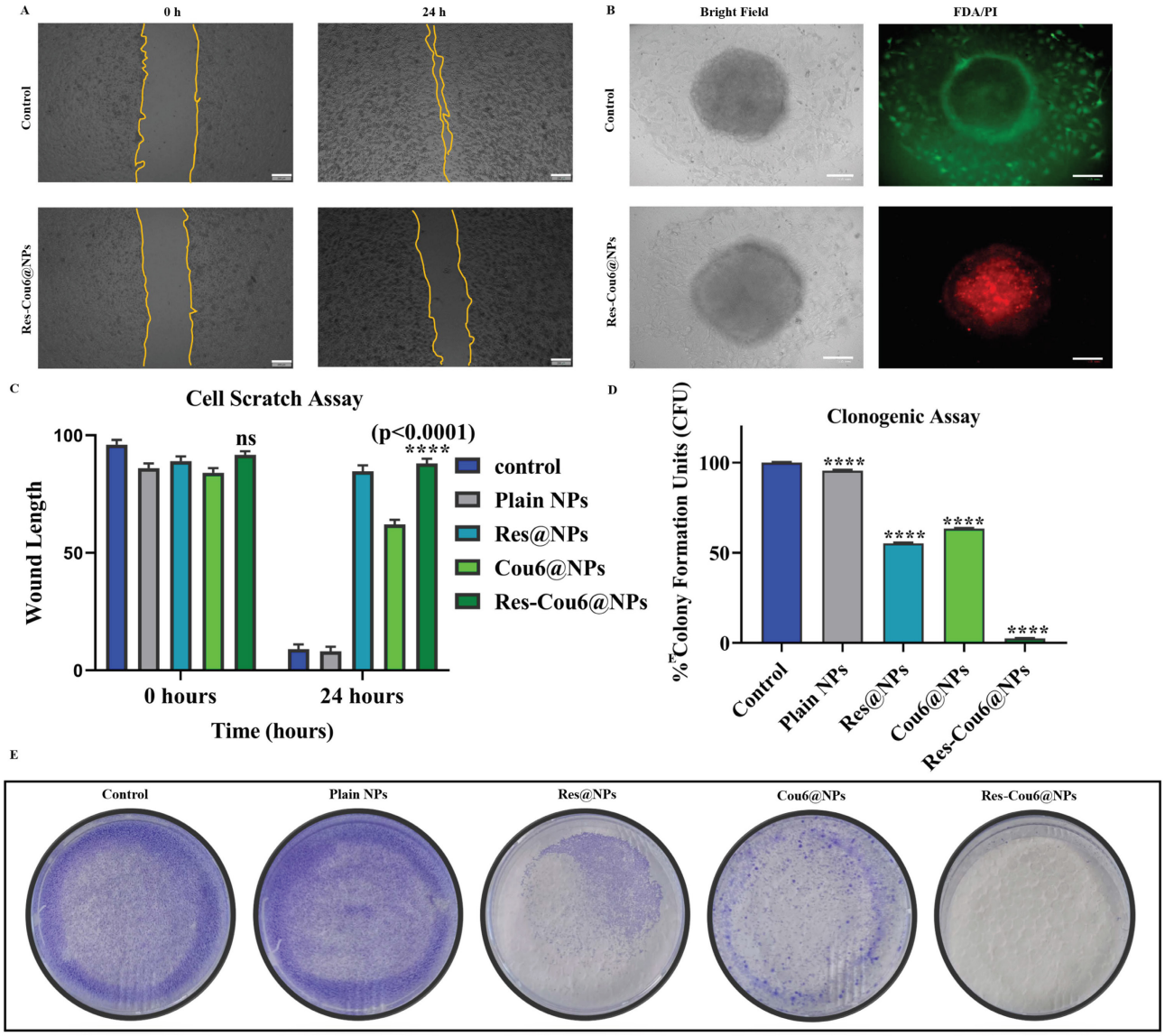


Figure 7. (A) Scratch closure estimation of Res-Cou6@NPs on melanoma cells estimated for 24 h (Scale bar: 200 μm) (B) 3D spheroid model for the live-dead analysis of Res-Cou6@NPs on B16F10 melanoma spheroids (scale bar: 100 μm) (C) Quantification analysis of scratch assay of Plain NPs, Res@NPs, Cou6@NPs, and Res-Cou6@NPs reported for 0, 6, 12, and 24 h (D) Quantification analysis of colony formation assay of Plain NPs, Res@NPs, Cou6@NPs, and Res-Cou6@NPs (E) Clonogenic assay of Plain NPs, Res@NPs, Cou6@NPs, and Res-Cou6@NPs treated B16F10 melanoma cells, untreated cells served as a control. Data are presented as mean ± SD (n = 3 independent biological replicates).

4.12 Clonogenic Assay

A clonogenic assay was conducted to evaluate the long-term proliferative capacity of B16F10 melanoma cells following treatment with nanoparticles. Cells were exposed to Plain NPs, Res@NPs, Cou6@NPs, or Res-Cou6@NPs for 24 h, then trypsinized and re-seeded in 35 mm plates for 7-day colony development monitoring. Results demonstrated significantly reduced colony formation in Res-Cou6@NPs-treated cells relative to controls (Figures 7D and 7E), indicating irreversible cytotoxicity and suppressed tumorigenic recurrence. This verifies the nanoformulation's effectiveness in eliminating clonogenic survival, an essential measure for the therapeutic destruction of malignant cells.

4.13 3D Spheroid Formation Assay

Three-dimensional spheroid models accurately replicate the tumor microenvironment *in vitro*, demonstrating of key characteristic of *in vivo* solid tumors, such as multicellular layering, structural organization, nutritional gradients, and hypoxia. These traits facilitate treatment resistance by enhancing drug efflux mechanisms and hypoxia adaption. Addressing the hypoxic core, a central point of drug resistance, metastatic potential, and angiogenic signaling, is a crucial therapeutic strategy. This research assesses the kinetics of drug release and the geographic distribution within tumor-mimetic

spheroids [70,71]. Res-Cou6@NPs shown considerable effectiveness against B16F10 melanoma spheroids. After exposure to Plain NPs, Res@NPs, Cou6@NPs, and Res-Cou6@NPs, both untreated controls and Plain NPs demonstrated minimal cytotoxicity. Res@NPs and Cou6@NPs induced only peripheral cytotoxicity (Figure S10c), attributable to limited penetration capacity and hydrophobic confinement. Conversely, Res-Cou6@NPs inflicted extensive damage progressing radially from the periphery to the hypoxic core (Figure 7B), indicating deep tumor-penetrating capability.

4.14 Immunofluorescence

To determine whether Res-Cou6@NPs enhance the radiosensitivity of B16F10 melanoma cells by promoting DNA damage, the extent of DNA double-strand breaks (DSBs) was examined by quantifying γ-H2AX foci through immunofluorescence staining conducted 12 h post-irradiation. Representative fluorescence images (Fig. 9A) revealed a noticeable increase in γ-H2AX foci in cells pretreated with Res@NPs, Cou6@NPs, and particularly Res-Cou6@NPs, compared to cells exposed to radiation alone (control groups shown in Fig. S13). The fluorescence intensity corresponding to γ-H2AX foci was quantified, and statistical evaluation was performed using two-way ANOVA (Fig. 9B). The results demonstrated that pretreatment with Res-Cou6@NPs led to a significant elevation in radiation-induced γ-H2AX foci relative to other control groups [72].

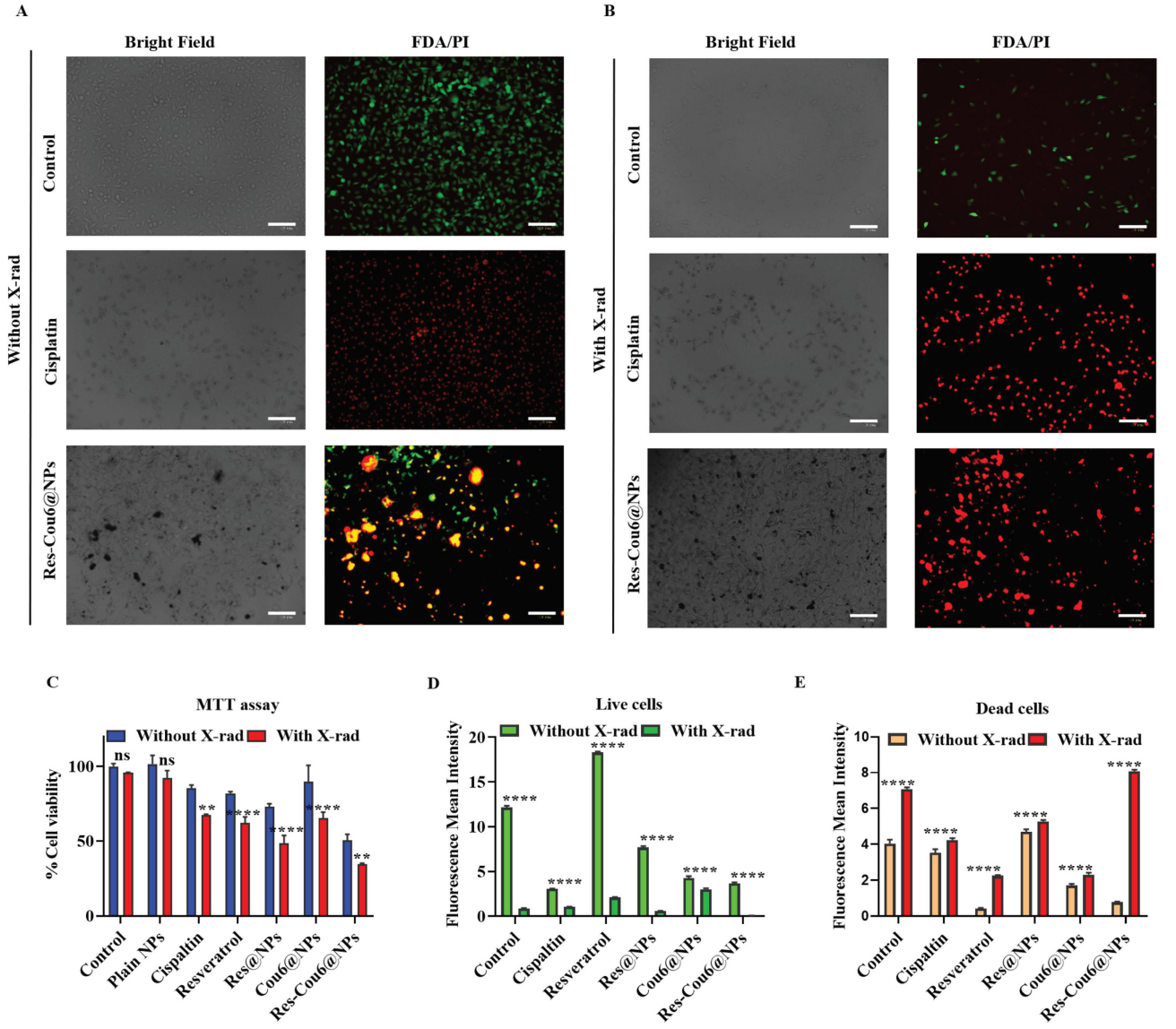


Figure 8. (A) Live/Dead assay in melanoma cells after treatment with Cisplatin, and Res-Cou6@NPs (Without x-ray) (scale bar: 100 μm) (B) Live/Dead assay in B16F10 melanoma cells after treatment with Cisplatin, and Res-Cou6@NPs (With x-ray) (scale bar: 100 μm) (C) MTT assay of Cisplatin, Resveratrol, Res@NPs, Cou6@NPs, and Res-Cou6@NPs, with and without X-ray (D, E) Quantification analysis for Live/Dead assay of Cisplatin, Resveratrol, Res@NPs, Cou6@NPs, and Res-Cou6@NPs. Data are presented as mean ± SD (n = 3 independent biological replicates).

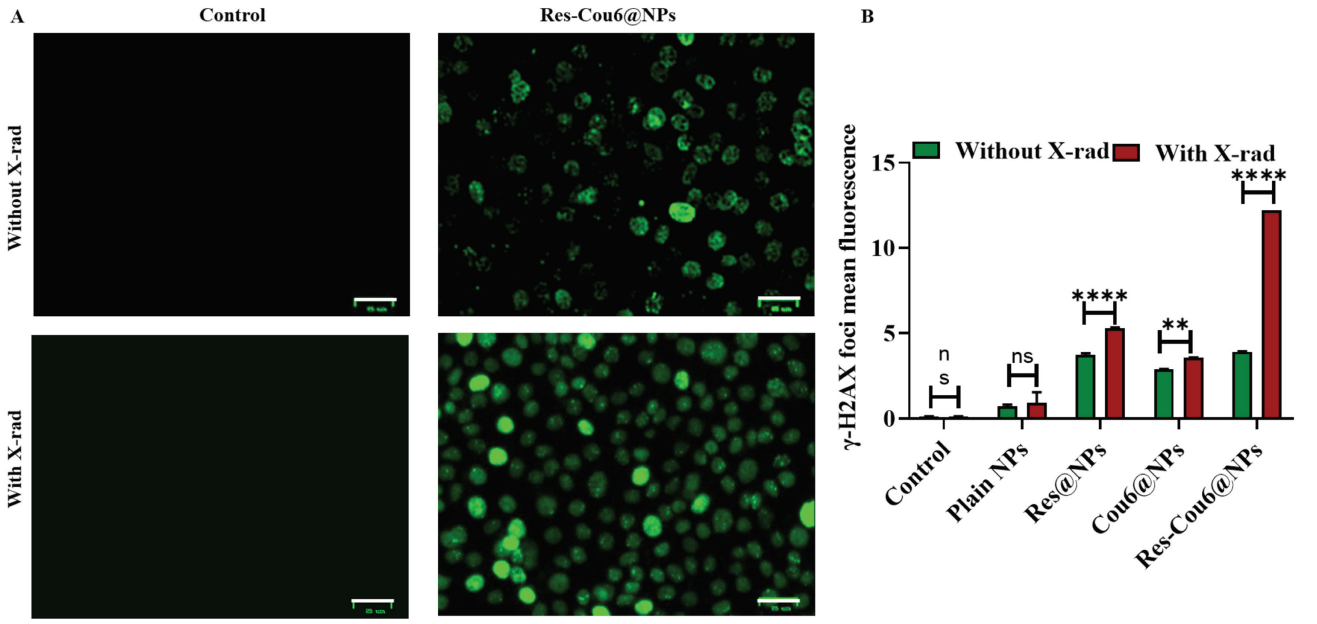


Figure 9. Res-Cou6@NPs enhances radiation-induced DNA DSBs in Melanoma cells. (A) Representative immunofluorescence images of γ-H2AX foci (green) in melanoma cells without X-rad and with X-rad followed by irradiation with 4 Gy at a dose rate of 0.8 Gy·min^{-1} over 5 minutes (scale bar: 25 μm). (B) Quantification of the γ-H2AX foci mean fluorescence. Data are presented as mean ± SD (n = 3 independent biological replicates).

The main aim of this nanoplatform is to examine the capacity of Resveratrol-based nanoformulations to surmount innate radioresistance, rather than only acting as a cytotoxic agent. Our research indicates that Resveratrol, when co-administered with Coumarin-6 in nanoparticle formulation (Res-Cou6@NPs), displays significant radiosensitizing effects in both radioresistant models (bacteria and human). *In vitro* experiments shown that pretreatment with Res-Cou6@NPs markedly decreased cell viability post-irradiation, exhibiting a more pronounced augmentation of radiation-induced damage relative to radiation exposure alone. Cells subjected to a cumulative radiation exposure of 4 Gy at a dose rate of 0.8 Gy·min^{-1} over 5 minutes demonstrated significantly enhanced cytotoxic reactions in the presence of Res-Cou6@NPs, highlighting the radiosensitizing capability of the formulation rather than a dose-dependent lethality. Live/Dead staining corroborated our results, indicating substantial radiation-induced cytotoxicity with nanoparticle pretreatment, hence implying increased radiation efficacy. Increased γ-H2AX foci development showed that there were more DNA double-strand breaks (DSBs), which meant that the DNA repair process was less effective and the cells were less likely to survive after radiation. The observed radiosensitization is probably controlled by a number of interconnected processes, such as the rise in intracellular ROS caused by nanoparticles during irradiation, the disruption of redox homeostasis, and the interference with DNA damage response pathways.

The radiosensitizing effectiveness of Res-Cou6@NPs was further validated employing *Deinococcus radiodurans*, a well-established model organism renowned for its exceptional radioresistance. The nanoformulation treatment significantly exacerbated radiation-induced damage in these resilient bacteria, highlighting the capacity of Res-Cou6@NPs to impair robust DNA repair and antioxidant defense mechanisms. A dose of 4 Gy of radiation was chosen on purpose as a realistic preclinical exposure to show sensitization effects without aiming for the highest possible death rate. This work shows that Res-Cou6@NPs are a good way to make cells more sensitive to radiation. They can change how radiation affects cells in a wide range of species that are quite resistant to it. More research using different levels of radiation, fractionation methodologies, and mechanistic bacterial assays will help us understand this radiosensitization strategy better and make it more useful in the real world.

The present study illustrates encouraging *in vitro* radiosensitization with the synthesized liposomal nanoplatform; however, numerous obstacles persist prior to its effective clinical application. This encompasses attaining consistent large-scale production, validating formulation stability, investigating *in vivo* biodistribution, pharmacokinetics, systemic toxicity, immune interactions, and fulfilling regulatory standards. Furthermore, the physicochemical properties of the nanoplatform, especially its particle size (~200 nm), are anticipated to significantly influence its *in vivo*

performance. Nanoparticles of this size are typically seen as advantageous for passive tumor accumulation via the EPR phenomenon, while minimizing the swift renal clearance linked to smaller nanoparticles. Nonetheless, particle dimensions may additionally affect circulation duration, digestion by the mononuclear phagocyte system, and organ distribution, all of which necessitate thorough assessment under physiological circumstances. Nonetheless, the application of biocompatible lipid-based nanocarriers offers a promising foundation for clinical implementation due to their recognized safety record and adaptability in drug administration. Consequently, forthcoming research will concentrate on thorough *in vivo* examinations, encompassing pharmacokinetic assessment, biodistribution, tumor retention, biosafety appraisal, and therapeutic effectiveness in appropriate animal models to further validate the translational viability of the formulated product.

5. Conclusion

In summary, we report a multifunctional liposomal nanoplatform (Res-Cou6@NPs) for efficient radiosensitizer delivery, exhibiting nanoscale uniformity, structural stability, and effective biological performance. The system demonstrated a pronounced ability to enhance radiation-induced damage, as evidenced by increased membrane disruption and reduced survival in the radiation-resistant model organism *Deinococcus radiodurans*. Importantly, this enhanced radiosensitization was recapitulated in mammalian systems, where Res-Cou6@NPs promoted ROS generation, mitochondrial dysfunction, and apoptosis in melanoma cells, while inhibiting migration, clonogenic survival, and three-dimensional spheroid invasion, with minimal effects on normal fibroblasts. These findings highlight the potential of the developed liposomal nanoplatform as an effective biomaterial-based radiosensitizer, capable of overcoming intrinsic radioresistance across biological systems. Furthermore, the integration of a radiation-resistant microbial model as a pre-screening tool provides a complementary strategy for evaluating nanomedicine performance under stringent conditions. Overall, this work offers a biomaterial-centered approach for enhancing radiotherapeutic efficacy and supports the development of next-generation radiosensitizing nanoplatforms, with future studies aimed at *in vivo* validation and therapeutic translation.

Supplementary Material

Supplementary figures and table.
https://www.ntno.org/v10p0317s1.pdf

Acknowledgments

A.K.R. thanks ICMR-IIRPIG/2024/01/2351, ICMR-FIW-2024-1-208-B, ICMR-CoE, SUPRA (SPR/2022/000230), ANRF-ARG-2025/008857/LS, MoE/STARS (STARS 2/2023-640), MoE/ SPARC/P2082 and IITH/BME/SOCH3 for the financial support. The author N.B. thanks the University Grants Commission (UGC), Government of India, for the UGC-JRF fellowship- 18-340769. The authors C.L.P. and T.L.S. thank MHRD for funding their fellowship. Biorender.com was used for the illustrations of this research article.

Authorship Contribution Statement

Nitisha Beniwal: Software, Experiments, Conceptualization, Examination, Procedure, Validation, writing - original draft & reviewing; **Chandra Lekha Putta:** Experimentation, Formal analysis, Data Acquisition, Reviewing, and Editing; **Thaninki Lakshmi Srujana:** *Deinococcus radiodurans* experiments, investigation, and Data Acquisition, Reviewing and Editing.

Competing Interests

An Indian Patent has been granted for the work (Patent No. 582482).

References

1. Farasatkia A, Maeso L, Gharibi H, Dolatshahi-Pirouz A, Stojanovic GM, Antezana PE, et al. Design of nanosystems for melanoma treatment. Int J Pharm. 2024;665:124701.
2. Bezrookove V, Kianian S, McGeever L, Jones R, Caressi C, Nosrati M, et al. The molecular evolution of melanoma distant metastases. J Investig Dermatol. 2024;144(11):2530-2540.e1.
3. Lallas K, Kyrgidis A, Chrysostomidis A, Vakirlis E, Apalla Z, Lallas A. Clinical, dermatoscopic, histological and molecular predictive factors of distant melanoma metastasis: A systematic review and meta-analysis. Crit Rev Oncol Hematol. 2024;202:104458.
4. DeBusk L, Rosenberg A, Burshtein J, Shah M, Zakria D, Bartley B, et al. Radiation therapy for metastatic melanoma. Dermatol Clin. 2025;43(3):495-501.
5. Zhang Y, Han X, Liu Y, Wang S, Han X, Cheng C. Research progress on nano-sensitizers for enhancing the effects of radiotherapy. Mater Adv. 2022;3(9):3709-3725.
6. Bemidinezhad A, Mirzavi F, Gholamhosseinian H, Gheybi F, Soukhtanloo M. Gold-containing liposomes and glucose-coated gold nanoparticles enhances the radiosensitivity of B16F0 melanoma cells via increasing apoptosis and ROS production. Life Sci. 2023;318:121495.
7. Salehi F, Daneshvar F, Karimi M, Dehdari Vais R, Mosleh-Shirazi MA, Sattarahmady N. Enhanced melanoma cell-killing by combined phototherapy/radiotherapy using a mesoporous platinum nanostructure. Photodiagnosis Photodyn Ther. 2019;28:300-307.
8. Biran R, Pond D. Heparin coatings for improving blood compatibility of medical devices. Adv Drug Deliv Rev. 2017;112:12-23.
9. Carter LG, D'Orazio JA, Pearson KJ. Resveratrol and cancer: focus on in vivo evidence. Endocr Relat Cancer. 2014;21(3):R209-R225.
10. Wiegner EA, King CR. Sexual function after stereotactic body radiotherapy for prostate cancer: results of a prospective clinical trial. Int J Radiat Oncol Biol Phys. 2010;78(2):442-448.
11. Danhier F, Ansorena E, Silva JM, Coco R, Le Breton A, Préat V. PLGA-based nanoparticles: an overview of biomedical applications. J Control Release. 2012;161(2):505-522.
12. Miyake M, Kamada N, Oka Y, Mukai T, Minami T, Toguchi H, et al. Development of suppository formulation safely improving rectal absorption of rebamipide, a poorly absorbable drug, by utilizing sodium laurate and taurine. J Control Release. 2004;99(1):63-71.
13. Marinović M, Poje G, Perković I, Fontinha D, Prudêncio M, Held J, et al. Further investigation of harmicines as novel antiplasmodial agents: Synthesis,

structure-activity relationship and insight into the mechanism of action. Eur J Med Chem. 2021;224:113687.
14. Sezgin Bayindir Z, Sova M, Yuksel N, Saso L. Delivery strategies to improve the pharmacological efficacy of NRF2 modulators: a review. RSC Med Chem. 2025;16:4599-4616.
15. Yang S, Li Z, Li S, Zhang J, Huang J, Ren J, et al. Advances in drug delivery systems based on liposome-composite hydrogel microspheres. J Mater Chem B. 2025;13(38):11885-11908.
16. Hogarth C, Arnold K, McLauchlin A, Rannard SP, Siccardi M, McDonald TO. Evaluating the impact of systematic hydrophobic modification of model drugs on the control, stability and loading of lipid-based nanoparticles. J Mater Chem B. 2021;9(48):9874-9884.
17. Chakraborty B, Patel G, Padhan B, Das J, Patel M. Evolution of lipid nanoparticles as charioteers of Alzheimer's disease therapeutics. Appl Mater Today. 2024;41:102442.
18. Song M, Zhu B, Qiu S, Tian J, Li J, Chen D, et al. Codelivery of afuresertib and celecoxib by IL4RPep-1-targeting nanoparticles for effective treatment against melanoma. Appl Mater Today. 2023;33:101868.
19. Wang H, Liu Y, He R, Xu D, Zang J, Weeranoppanant N, et al. Cell membrane biomimetic nanoparticles for inflammation and cancer targeting in drug delivery. Biomater Sci. 2020;8(2):552-568.
20. Li Z, Li M, Lu J. Biomimetic liposomes in drug delivery: from design mechanisms to applications. Chem Soc Rev. 2026;55:1008-1038.
21. Goshisht MK, Goshisht A, Bajpai A, Bajpai A. Recent advances in biomedical applications of smart nanomaterials: a comprehensive review. RSC Pharm. 2025;2(6):1227-1267.
22. Kadian V, Dalal P, Kumar S, Kapoor A, Rao R. Comparative evaluation of dithranol-loaded nanosponges fabricated by solvent evaporation technique and melt method. Futur J Pharm Sci. 2023;9(1):13.
23. Marwah H, Garg T, Goyal AK, Rath G. Permeation enhancer strategies in transdermal drug delivery. Drug Deliv. 2016;23(2):564-578.
24. Priya S, Desai VM, Singhvi G. Surface modification of lipid-based nanocarriers: a potential approach to enhance targeted drug delivery. ACS Omega. 2023;8(1):74-86.
25. Sharifi-Rad J, Quispe C, Mukazhanova Z, Knut E, Turgumbayeva A, Kipchakbayeva A, et al. Resveratrol-based nanoformulations as an emerging therapeutic strategy for cancer. Front Mol Biosci. 2021;8:649395.
26. Gregoriou Y, Gregoriou G, Yilmaz V, Kapnisis K, Prokopi M, Anayiotos A, Strati K, Dietis N, Constantinou AI, Andreou C. Resveratrol loaded polymeric micelles for theranostic targeting of breast cancer cells. Nanotheranostics 2021; 5(1):113-124.
27. El-Benhawy SA, Morsi MI, Fahmy EI, Soula MA, Khalil FA, Arab AR. Role of resveratrol as radiosensitizer by targeting cancer stem cells in radioresistant prostate cancer cells (PC-3). Asian Pac J Cancer Prev. 2021;22(12):3823-3837.
28. Shen H, Shi S, Zhang Z, Gong T, Sun X. Coating solid lipid nanoparticles with hyaluronic acid enhances antitumor activity against melanoma stem-like cells. Theranostics. 2015;5(7):755-771.
29. Ren X, Xue R, Luo Y, Wang S, Ge X, Yao X, et al. Programmable melanoma-targeted radio-immunotherapy via fusogenic liposomes functionalized with multivariate-gated aptamer assemblies. Nat Commun. 2024;15:5035.
30. Solanki R, Rajput PK, Jodha B, Yadav UCS, Patel S. Enhancing apoptosis-mediated anticancer activity of evodiamine through protein-based nanoparticles in breast cancer cells. Sci Rep. 2024;14:2595.
31. Eswar K, Sankaranarayanan SA, Srivastava R, Harijan D, Prabusankar G, Rengan AK. Omeprazole-loaded copper nanoparticles for mitochondrial damage mediated synergistic anticancer activity against melanoma cells. ACS Appl Bio Mater. 2024;7(7):4795-4803.
32. Khatun S, Pebam M, Sankaranarayanan SA, Pogu SV, Bantal VS, Rengan AK. Glutathione-IR 797 coupled Casein Nano-Trojan for augmenting the therapeutic efficacy of camptothecin in highly invasive triple negative breast cancer. Biomater Adv. 2024;159:213802.
33. Sivandzade F, Bhalerao A, Cucullo L. Analysis of the mitochondrial membrane potential using the cationic JC-1 dye as a sensitive fluorescent probe. Bio Protoc. 2019;9(1):e3128.
34. Putta CL, Buddhiraju HS, Yadav DN, Basa A, Rengan AK. Baicalein and IR780 coloaded liposomes for antifungal and anticancer therapy. ACS Appl Bio Mater. 2025;8(1):661-675.
35. Pebam M, Khatun S, Ali MS, Srivastava A, Rengan AK. Self-assembled IR dye/mitoxantrone loaded Porphysomes nanosystem for enhanced combinatorial chemo-photothermal cancer therapy. Colloids Surf B Biointerfaces. 2024;241:113985
36. Franken NAP, Rodermond HM, Stap J, Haveman J, van Bree C. Clonogenic assay of cells in vitro. Nat Protoc. 2006;1(5):2315-2319.
37. Hua S, Zhao J, Li L, Liu C, Zhou L, Li K, et al. Photosynthetic bacteria-based whole-cell inorganic-biohybrid system for multimodal enhanced tumor radiotherapy. J Nanobiotechnol. 2024;22(1):379.
38. Rothe R, Xu Y, Wodtke J, Brandt F, Meister S, Laube M, et al. Programmable release of chemotherapeutics from ferrocene-based injectable hydrogels slows melanoma growth. Adv Healthc Mater. 2024;13(27):2400265.
39. Fu S, Chang L, Liu S, Gao T, Sang X, Zhang Z, et al. Temperature sensitive liposome based cancer nanomedicine enables tumour lymph node immune microenvironment remodelling. Nat Commun. 2023;14(1):2248.
40. Yuan J, Chen Q, Zuo M, Li X, Ou CY, Chen Q, et al. Enhanced combination therapy through tumor microenvironment-activated cellular uptake and ROS-sensitive drug release using a dual-sensitive nanogel. Biomater Sci. 2025;13(6):1554-1567.
41. Liu C, Xu W, Song X, Tian W, Liu F, Wang F. A nanotheranostic agent for synergistic antitumor chemo/phototherapy prepared by paclitaxel-induced self-assembly of PEGylated human serum albumin with prolonged circulation. ACS Omega. 2024;9(52):51062-51072.
42. Zhang M, Gao S, Yang D, Fang Y, Lin X, Jin X, et al. Influencing factors and strategies of enhancing nanoparticles into tumors in vivo. Acta Pharm Sin B. 2021;11(8):2265-2285.
43. Nguyen CNM, Nguyen SH, Tran MT. Nanoparticles in cancer therapy: Strategies to penetrate and modulate the tumor microenvironment – a review. Smart Mater Med. 2025;6(2):270-284.
44. Öztürk K, Kaplan M, Çalış S. Effects of nanoparticle size, shape, and zeta potential on drug delivery. Int J Pharm. 2024;666:124799.
45. Kumar M, Kulkarni P, Liu S, Chemuturi N, Shah DK. Nanoparticle biodistribution coefficients: A quantitative approach for understanding the tissue distribution of nanoparticles. Adv Drug Deliv Rev. 2023;194:114708.
46. Hindarto CK, Surini S, Permana AH, Redjeki S, Irawan C. Effect of mole ratio on physicochemical properties of luteolin-loaded phytosome. Pharma Innovation. 2017;6(12):96-101.
47. Danaei M, Dehghankhold M, Ataei S, Hasanzadeh Davarani F, Javanmard R, Dokhani A, et al. Impact of particle size and polydispersity index on the clinical applications of lipidic nanocarrier systems. Pharmaceutics. 2018;10(2):57.
48. Vadlapatla RK, Vadlapudi AD, Kwatra D, Pal D, Mitra AK. Differential effect of P-gp and MRP2 on cellular translocation of gemifloxacin. Int J Pharm. 2011;420(1):26-33.
49. Franco MS, Gomes ER, Roque MC, Oliveira MC. Triggered drug release from liposomes: exploiting the outer and inner tumor environment. Front Oncol. 2021;11:623760.
50. Alrbyawi H, Poudel I, Annaji M, Boddu SHS, Arnold RD, Tiwari AK, et al. pH-sensitive liposomes for enhanced cellular uptake and cytotoxicity of daunorubicin in melanoma (B16-BL6) cell lines. Pharmaceutics. 2022;14(6):1128.
51. Neves AR, Martins S, Segundo MA, Reis S. Nanoscale delivery of resveratrol towards enhancement of supplements and nutraceuticals. Nutrients. 2016;8(3):131.
52. Gillies RJ, Gatenby RA. Hypoxia and adaptive landscapes in the evolution of carcinogenesis. Cancer Metastasis Rev. 2007;26(2):311-317.
53. Kou L, Sun J, Zhai Y, He Z. The endocytosis and intracellular fate of nanomedicines: implication for rational design. Asian J Pharm Sci. 2013;8(1):1-10.
54. Singh SP, Alvi SB, Pemmaraju DB, Singh AD, Manda SV, Srivastava R, et al. NIR triggered liposome gold nanoparticles entrapping curcumin as in situ adjuvant for photothermal treatment of skin cancer. Int J Biol Macromol. 2018;110:375-382.
55. Han HS, Koo SY, Choi KY. Emerging nanoformulation strategies for phytocompounds and applications from drug delivery to phototherapy to imaging. Bioact Mater. 2022;14:182-205.
56. Yusuf A, Almotairy ARZ, Henidi H, Alshehri OY, Aldughaim MS. Nanoparticles as drug delivery systems: a review of the implication of nanoparticles' physicochemical properties on responses in biological systems. Polymers (Basel). 2023;15(7):1596.
57. Jeevanandam J, Chan YS, Danquah MK. Nano-formulations of drugs: recent developments, impact and challenges. Biochimie. 2016;128-129:99-112.
58. Wongrakpanich A, Bui Thi Thu H, Sakchaisri K, Taresco V, Cuzzucoli Crucitti V, Bunsupa S, Suksiriworapong J. Co-delivery of curcumin and resveratrol by folic acid-conjugated poly(glycerol adipate) nanoparticles for enhanced synergistic anticancer effect against osteosarcoma. J Drug Deliv Sci Technol. 2024;95:105610.
59. Patial V, Mahesh S, Sharma S, Pratap K, Singh D, Padwad YS. Synergistic effect of curcumin and piperine in suppression of DENA-induced hepatocellular carcinoma in rats. Environ Toxicol Pharmacol. 2015;40(2):445-452.
60. Červinka M, Bereiter-Hahn J, Peychl J, Rudolf E, Cervinková Z. The role of mitochondria in apoptosis induced in vitro. Gen Physiol Biophys. 1999;18(Spec No):33-40.
61. Heo JR, Kim SM, Hwang KA, Kang JH, Choi KC. Resveratrol induced reactive oxygen species and endoplasmic reticulum stress-mediated apoptosis, and cell cycle arrest in the A375SM malignant melanoma cell line. Int J Mol Med. 2018;42(3):1427-1435.
62. Posadino AM, Giordo R, Cossu A, Nasrallah GK, Shaito A, Abou-Saleh H, et al. Flavin oxidase-induced ROS generation modulates PKC biphasic effect of resveratrol on endothelial cell survival. Biomolecules. 2019;9(6):209.
63. Wang X, Shen T, Lian J, Deng K, Qu C, Li E, et al. Resveratrol reduces ROS-induced ferroptosis by activating SIRT3 and compensating the GSH/GPX4 pathway. Mol Med. 2023;29(1):137.
64. Zhou X, Chen M, Zeng X, Yang J, Deng H, Yi L, et al. Resveratrol regulates mitochondrial reactive oxygen species homeostasis through Sirt3 signaling pathway in human vascular endothelial cells. Cell Death Dis. 2014;5(12):e1576.
65. Widlund AL, Baral K, Dalgaard LT, Vang O. Functional mitochondria are important for the effect of resveratrol. Molecules. 2017;22(5):847.
66. Ye M, Wu H, Li SG. Resveratrol alleviates oxygen/glucose deprivation/reoxygenation-induced neuronal damage through induction of mitophagy. Mol Med Rep. 2021;23(1):73.

67. Ragonese F, Monarca L, De Luca A, Mancinelli L, Mariani M, Corbucci C, et al. Resveratrol depolarizes the membrane potential in human granulosa cells and promotes mitochondrial biogenesis. Fertil Steril. 2021;115(4):1063-1073.
68. Arozarena I, Wellbrock C. Targeting invasive properties of melanoma cells. FEBS J. 2017;284(14):2148-2162.
69. Ju RJ, Stehbens SJ, Haass NK. The role of melanoma cell-stroma interaction in cell motility, invasion, and metastasis. Front Med (Lausanne). 2018;5:307.
70. Riffle S, Hegde RS. Modeling tumor cell adaptations to hypoxia in multicellular tumor spheroids. J Exp Clin Cancer Res. 2017;36(1):102.
71. Mehta G, Hsiao AY, Ingram M, Luker GD, Takayama S. Opportunities and challenges for use of tumor spheroids as models to test drug delivery and efficacy. J Control Release. 2012;164(2):192-204.
72. Wang L, Lin H, Yin L, Gou Q, Ji Y. Biomimetic nanoparticles facilitate homologous targeting and radiosensitivity in glioblastoma cells. Mater Today Nano. 2025;32:100676.